Lecture presented at International School of Electron Microscopy (Center for Scientific Culture), Erice, Trapani, Sicily, April 7-21, 1973

LBL-1471

INTRODUCTION TO TRANSMISSION ELECTRON MICROSCOPY

Gareth Thomas

April 1973

Prepared for the U. S. Atomic Energy Commission
under Contract W-7405-ENG-48

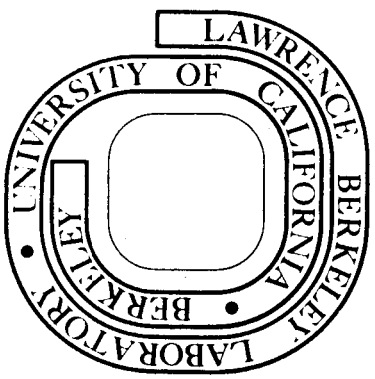

DISCLAIMER

ERICE SCHOOL

April 1973

INTRODUCTION TO TRANSMISSION ELECTRON MICROSCOPY

Gareth Thomas
Professor of Metallurgy
Department of Materials Science and Engineering
University of California
Berkeley, California 94720

CHAPTER 1

GEOMETRY OF ELECTRON DIFFRACTION

1. INTRODUCTION

a. Basis for Electron Microscopy

The information that is obtained by electron microscopical methods (Fig. 1) is derived from the scattering processes that take place when the electron beam travels through the specimen. There are two main types of scattering a) elastic - the interaction of the electrons and the effective potential field of the nuclei - involving no energy loses and which can be coherent or incoherent (poor phase relationships) b) inelastic - the interaction of the electrons and the electrons in the specimen involving energy losses and absorption. It is the elastic scattering that produces a diffraction pattern; and if the scattering centers in the specimen are arrayed in an orderly, regular manner such as in crystals, the scattering is coherent and results in spot patterns, kikuchi patterns and, if the sample is a fine grained polycrystal, ring patterns.

When an image is formed of the scattered beams, two main mechanisms of contrast arise. If the transmitted and scattered beams can be made to recombine, so preserving their amplitudes and phases, then a lattice image of the planes which are diffracting may be resolved directly (phase contrast). The principle is the same as that of the Abbé theory for gratings in light optics (see Fig. 2a-c). Alternatively, amplitude contrast is obtained by deliberately excluding the diffracted beams (and hence the phase relationships) form the imaging sequences by the use of suitably sized apertures, placed in the back focal plane of the objective lens (Fig 3). Such an image is called a bright field image. Alternatively, a dark field image can be obtained by excluding all beams except the particular diffracted beam of interest. Examples are given in Fig. 4.

We shall return to further considerations of this in the next chapter.

The basic reason for the utilization of the electron microscope is its superior resolution resulting from the very small wavelengths compared to other forms of radiation (light, x-rays, neutrons). The resolution is given by the Rayleigh formula which is derived from considering the maximum angle of electron scattering (α) which can pass through the objective lens. This formula is:

$$R = \frac{0.61\lambda}{\alpha} \qquad (1)$$

where R is the size of the resolved object, λ is wavelength, and α is identical to the effective aperture of the objective lens.

In the electron microscope, the effective aperture is limited chiefly by spherical aberration. The spherical aberration error is:

$$\Delta S = C_s \alpha^3 \qquad (2)$$

where C_s is the coefficient of spherical aberration of the objective lens (≈ focal length e.g. 3mm).

Thus R increases with decreasing α; whereas ΔS decreases with decreasing α. As a result, in electron optics one arrives at an optimum aperture and minimum aberration given by:

$$\alpha_{opt} = A(\lambda^{\frac{1}{4}})C_s^{-1/4} \qquad (3)$$

$$\Delta R_{min} = B(\lambda^{\frac{3}{4}})C_s^{1/4} \qquad (4)$$

where A,B are constants ≈ unity.

The relativistic wavelength of electrons depends on the accelerating voltage and is given by the modified DeBroglie wavelength:

$$\lambda = \frac{h}{\left[2m_o\, eE\left(1 + \frac{eE}{2m_o c^2}\right)\right]^{1/2}} \quad (5)$$

$$= \frac{12.26}{E^{1/2}(1+0.9788 \times 10^{-6}E)^{1/2}} \ (\text{Å})$$

where h = Planck's constant, m_o is rest mass and e the charge on the electron, E is the accelerating potential (volts), c is the velocity of light, v is the electron velocity.

and thus decreases with energy E. Some values pertinent to electron microscopy are given below in Table 1.

TABLE 1

E(volts)	λ(Å)	λ^{-1}(Å)$^{-1}$	$(v/c)^2$
80kV	0.0418	23.95	0.2524
100kV	0.037	27.02	0.3005
200kV	0.0251	39.87	0.4835
500kV	0.0142	70.36	0.7445
1 MeV	0.0087	114.7	0.8856
2 MeV	0.005	198.3	0.9586
10 MeV	0.0012	846.8	0.9976

Another advantage of the small wavelength of electrons is that the depth of field and depth of focus are very large in electron microscopes.

Thus, at 100 kV α(opt) $\approx 6\times10^{-3}$ rad. and ΔR min $\approx$ 6.5Å for C_s = 3.3 mm. Other factors which affect resolution are astigmatism and chromatic aberration of the imaging system, and chromatic aberration resulting from energy losses in the specimen. These errors produce poor resolution for non axial illumination, such as off axis aperture dark field imaging as can be seen by comparing Figures 3 and 4a,b,c. The chromatic disc of confusion is given by:

$$\Delta C = C_c \alpha \frac{\Delta E}{E} \qquad (6)$$

where C_c is the coefficient of chromatic aberration of the lens.

ΔE arises from voltage fluctuations in the incident beam, current fluctuations in the lenses, and absorption processes in the specimen. Whilst αopt and ΔR min change slowly with E (through λ) ΔC rapidly decreases with E and this is one of the main advantages of high voltage operation.

High voltage electron microscopy is now well established in many laboratories in different countries. High voltages are useful for several reasons (1-7). The effective scattering cross sections decrease with energy as indicated in Fig. 5. This predicts an improvement in specimen penetration for a given level of resolution, and is especially important for materials science. Experimentally, however, it is found that only in light materials (Si,Al) is there a significant gain in penetration as shown by Fig. 6. The reduction in inelastic scattering with increasing voltage implies a reduction in ionization and other damaging processes, and this has been observed for several biological and polymeric solids. However, knock-on damage occurs above a threshold energy which is roughly proportional to atomic number (e.g. ≃ 500kV for copper; 1 MeV for gold). A further gain from increasing the voltage is the rapid reduction in spherical aberration. This can be seen from equation (2), viz., $\Delta S \simeq C_s \alpha^3$ and since $C_s \simeq \lambda^{-1}$, $\Delta S \simeq \lambda^2$.

b. Diffraction

In crystals, Bragg diffraction occurs and equation (1) can be adapted to the special case when $\alpha = 2\theta$ where θ is the Bragg angle. Bragg's Law defines constructive interference when the path difference between waves scattered by successive parallel planes of atoms spaced d apart is equal to an integral number of wavelengths (phase difference is $2\pi/\lambda$ times path difference). If θ is the angle of incidence, then as shown in Fig. 7, the path difference between waves 1 and 2 is $2d \sin\theta$, hence Bragg's Law is:

$$2d \sin\theta = n\lambda \qquad (7)$$

where n is the order of reflection. Equation 7 is essentially the same as equation 1 where now R = d and neglecting the factor 0.61. The formation of images of lattice planes in crystals will now depend upon whether the recombination of a diffracted and the transmitted beam can occur or not. Thus if 2θ is the angle between the diffracted and transmitted beams $2\theta \leq \alpha$; and fringes will be formed of spacing $x = \lambda/2\theta$. Taking this into account, and noting that for small angles Bragg's Law can be written $2d\theta = \lambda$, and adjustment of the aberration equations 2,3,6 the minimum resolvable fringe spacing x = d is 2Å or better at 100 kV. An example for 3.14 Å lattice images in Si is shown in Fig. 2b. High resolutions can only be achieved by tilting the illumination so that the diffracted and transmitted beams straddle the optic axis symmetrically, since in this orientation, phase shifts from spherical and chromatic aberration cancel. Suitably sized objective apertures are used to select the beams for imaging (Fig. 2c). It also should be noted from equation (6) that chromatic errors due to energy losses in the specimen are minimized by using very thin specimens ($\simeq$ 100Å) and high voltages. Lattice imaging was introduced by Menter (8) and has recently been receiving considerable attention e.g., Komoda (9), Phillips (10), Allpress and Sanders (11). It is discussed further in this book by Howie.

Figure 2 shows that in all cases, the image is a magnified picture of the diffraction pattern whether the specimen is crystalline or truly amorphous. The diffraction pattern itself is formed in the back focal plane of the objective lens; and by suitable changes in magnification utilizing projector lenses of variable focal length, it is easy to quickly obtain images and their diffraction patterns on the fluorescent screen and record them photographically or display them on a monitor by TV techniques from which video recordings can be made. The principle of the electron microscope (Fig. 2) can be conveniently demonstrated by setting up an optical bench using a laser light source, and a series of glass lenses.

c. Selected Area Diffraction

The intermediate lens can be focused at the back focal plane of the objective thereby allowing the diffraction pattern to be observed on the screen and photographed. If an aperture diameter D is placed in the image plane (Fig. 2a), only electrons passing through an area D/M on the specimen can reach the final screen. (M is the magnification of the objective).

However, due to spherical aberration, the error in selection of the area for analysis can be appreciable. The minimum selected area ΔA is given by equation 2, replacing α by the Bragg angle θ, viz.,

$$\Delta A \simeq C_s \theta^3 \simeq C_s (\lambda/d)^3 \text{ for small angles.}$$

Since C_s varies approximately as λ^{-1} then ΔA varies as λ^2 and thus decreases rapidly with increasing voltage. For example, $\Delta A \simeq 2\mu$ at 100 kV and 0.02μ at 1 MeV. This illustrates another advantage for high voltage microscopy.

The smallest size aperture D normally used is 5μ (Fig. 17(b) was thus obtained) and considerable care must be exercised so as to correctly align the microscope with proper focussing.

2. BRAGG'S LAW AND THE RECIPROCAL LATTICE

From equation (7) and Table 1, we can see that for fast electrons the Bragg angles are very small. For example, for a cubic crystal with $a_o = 4\text{Å}$, the Bragg angle θ for the 200 reflection at 100kV = 0.037 ÷ 4 $\simeq 10^{-2}$ rad. or $\simeq 0.5°$ [$d_{200} = a_0/(h^2 + k^2 + \ell^2)^{1/2} = 2\text{Å}$]. This means that Bragg diffraction will occur only for those planes that lie with a few degrees or so from the incident beam. i.e. planes whose poles lie close to 90° to the incident beam. If $\bar{g}_1 \ldots \bar{g}_n$ are vectors perpendicular to the reflecting planes $\{hk\ell\}_1 \ldots\ldots \{hk\ell\}_n$ and [uvw] is the direction of the beam, then to a first approximation

$$[\vec{g}_1]\cdot[u\vec{v}w] = [\vec{g}_n]\cdot[u\vec{v}w] = 0 \qquad (8)$$

Thus the diffraction pattern will contain the vectors $\vec{g}$ lying normal to the beam. In terms of the sterographic projection we can determine the vectors $\vec{g}$ or the poles of the planes $\{hk\ell\}$ by drawing a great circle at 90° to the pole uvw. This great circle will contain the poles satisfying condition (8). Conversely, if one wishes to select a diffraction vector $\vec{g}$ = uvw, the great circle of [uvw] contains all the orientations which contain that particular $\vec{g}$. This is illustrated for cubic crystals by the standard projection shown in Fig. 8.

The vectors g normal to the reflecting planes are called reciprocal lattice vectors. They have magnitude equal to the reciprocal of the d spacings of the particular hkℓ planes involved and terminate at reciprocal lattice points (relpoints), see Fig. 9

$$\text{Thus } |\vec{g}| = \frac{1}{d} = \frac{\sqrt{h^2+k^2+\ell^2}}{a_0} \quad \text{for cubic crystals.} \qquad (9)$$

If a*, b*, c* are the basis vectors of the reciprocal lattice, then relative to a point chosen as the origin, every other reciprocal lattice point can be reached by a reciprocal lattice vector of the form:

$\vec{g} = h\vec{a}^* + k\vec{b}^* + \ell\vec{c}^*$ where h,k,ℓ are always integers, identical to the Miller indices of the reflecting planes.

In the diffraction of radiation by crystals, each reciprocal lattice point is associated with a diffracted beam whose intensity is proportional to the shape, volume and perfection of the crystal and the geometrical structure Factor F_g for the unit cell defined by:

$$F_g = \sum_n f_i \exp\left[2\pi i\, \bar{g}_{(hk\ell)} \cdot \bar{r}_i\right] \quad (10)$$

where f is the atomic scattering factor for electrons for each atom in the structure, and $\bar{r}_i$ the vector position of the ith atom in the unit cell. The vector $\bar{r}$ is given by:

$$\bar{r} = u\bar{a} + v\bar{b} + w\bar{c}$$

where u,v,w are the coordinates of an atom in the unit cell of basis vectors $\bar{a},\bar{b},\bar{c}$

Thus $\bar{g}\cdot\bar{r} = (ha^* + kb^* + \ell c^*) \cdot (u\bar{a} + v\bar{b} + w\bar{c})$

$= hu + kv + \ell w$ (since $aa^* = bb^* = cc^* = 1$

$=$ integral

Thus "allowed" reflecting planes are those for which $F_g \neq 0$. For example for the simplest fcc lattice (e.g. Al,Cu,γ-Fe) there are four atoms of the same kind per cell at coordinates 000, $\frac{1}{2}\frac{1}{2}0$, $\frac{1}{2}0\frac{1}{2}$, $0\frac{1}{2}\frac{1}{2}$

$$\text{thus } F = f\left[1 + e^{\pi i(h/2 + k/2)} + e^{\pi i(h/2 + \ell/2)} + e^{\pi i(k/2 + \ell/2)}\right]$$

remembering that $e^{\pi i} = e^{3\pi i} = -1$ and $e^{2\pi i} = e^{4\pi i} = +1$

then F = 0 if h, k, ℓ are mixed (even and odd) integers

F = 4f if h, k, ℓ are unmixed

Thus, the reciprocal lattice corresponding to diffraction includes only the points for which $F \neq 0$ (Fig. 9). Table 2 summarizes F values for some simple lattices:

TABLE 2

Geometrical Structure Factor Rules for Basic Cells Containing only 1 Kind of Atomic Species.

Primitive	All Values h,k,ℓ	F = f (1 atom per cell)
Body Centered	(h+k+ℓ) even	F = 2f (2 atoms per cell)
Face Centered	h,k,ℓ unmixed	F = 4f (4 atoms per cell)
Base Centered (e.g. ab face)	h,k,ℓ unmixed	F = 2f (2 atoms per cell
Hexagonal c.p.	h+2k=3n, ℓ odd	F = 0 e.g. 0001
	h+2k=3n, ℓ even	F = 2f e.g. 0002
	h+2k=3n±1, ℓ odd	F = $\sqrt{3}$f e.g. 01$\bar{1}$1
	h+2k=3n±1, ℓ even	F = f e.g. 01$\bar{1}$0

For cubic crystals these results are summarized in Table 3. The last column will be useful when diffraction patterns are to be indexed.

Since $2d \sin\theta = n\lambda$, $\sin\theta = n\lambda/2d$ hence the sequence of order of reflections goes as $h^2 + k^2 + \ell^2$ (i.e. the smallest Bragg angle for reflection in BCC crystals corresponds to that for the 110 reflection), as listed in Table 3. Thus 220 is the second order reflection of 110 in the BCC system (n = 2).

For hexagonal crystals, it is recommended that the Miller-Bravais four index notation be used; and it is especially helpful if all crystallographic data are expressed in direction indices. Details are given in Reference 12.

TABLE 3

Allowed {hkℓ} values for cubic crystals *

BCC		FCC		D.C.		
$h^2+k^2+\ell^2$	hkℓ	$h^2+k^2+\ell^2$	hkℓ	$h^2+k^2+\ell^2$	hkℓ	$\sqrt{h^2+k^2+\ell^2}$
2	110					1.414
		3	111	3	111	1.732
4	200	4	200			2.000
6	211					2.449
8	220	8	220	8	220	2.828
10	310					3.162
		11	311	11	311	3.317
12	222	12	222			3.464
14	321					3.742
16	400	16	400	16	400	4.000
18	411,330					4.243
		19	331	19	331	4.359
20	420	20	420			4.472
22	332					4.690
24	422	24	422	24	422	4.899
26	431,510					5.099
		27	511, 333	27	511, 333	5.196
30	521					5.477
32	440	32	440	32	440	5.659

* $[h^2+k^2+\ell^2]$ has all possible values except $4^p(8n + 7)$ where p,n are integers including zero, thus e.g. 7, 15, 23 are not possible.

3. INDEXING DIFFRACTION PATTERNS

If a sphere of radius λ^{-1} is drawn from the specimen so as to pass through the origin of the reciprocal lattice, then it can be seen from Fig. 7 that the reciprocal lattice vector $\vec{g} = 0^*B$ will lie on this sphere if $\sin\theta = \left(|\vec{g}|/2\right) \div \left(\frac{1}{\lambda}\right)$, that is $2d \sin\theta = \lambda$, since $|\vec{g}| = d^{-1}$. Thus an alternative way of describing Bragg's law is to state that diffraction can only occur when the reflecting sphere passes through (or very close to) a reciprocal lattice point for which $F \neq 0$ (Fig. 9).

As shown in Table 1, the reflecting sphere for high energy electrons has a very large radius and a number of reciprocal lattice points from the same reciprocal lattice section can be quite close to the reflecting sphere and be observed on an electron diffraction pattern. Because of this fact, very little distortion of angles between reciprocal lattice vectors or of lengths of reciprocal lattice vectors occurs for high energy electrons. This makes electron diffraction patterns very easy to analyse; all that is needed is a ruler, a compass, and a slide rule.

The ratio between two reciprocal lattice vectors is

$$\frac{g_1}{g_2} = \frac{\frac{1}{d_1}}{\frac{1}{d_2}} = \frac{d_2}{d_1} . \qquad (13)$$

Restricting our attention to the cubic systems:

$$\frac{g_1}{g_2} = \frac{d_2}{d_1} = \frac{\sqrt{h_1^2 + k_1^2 + \ell_1^2}}{\sqrt{h_2^2 + k_2^2 + \ell_2^2}} , \qquad (14)$$

where $h_1k_1\ell_1$ and $h_2k_2\ell_2$ are the Miller indices of the two diffracting planes giving rise to the spots on the diffraction pattern, g_1 and g_2. For example, in the fcc system, the [112] diffraction pattern for electrons will be a rectangular network of points lying on the reciprocal lattice section normal to $[11\bar{2}]$ and containing the origin of reciprocal space. This can be seen by drawing the 112 plane in Fig. 9. The two shortest reciprocal lattice vectors will be in the ratios

$$\frac{g_1}{g_2} = \frac{\sqrt{3}}{\sqrt{8}} = \frac{\sqrt{1^2 + 1^2 + 1^2}}{\sqrt{2^2 + 2^2 + 0^2}} \qquad (15)$$

From Table 3 it can be seen that these arise from planes of the form $\{111\}$ and $\{220\}$. The signs on the indices and the positions of the indices in the brackets must now be chosen such that: (a) the indices are so arranged and signed that both reciprocal lattice vectors are normal to [112] and (b) the angle between the two reflecting planes matches the measured angle between the two reciprocal lattice vectors, i.e.,

$$\cos\theta = \frac{\vec{g}_1 \cdot \vec{g}_2}{|g_1|\,|g_2|} = \cos(\vec{g}_1, \vec{g}_2) = 90°. \qquad (16)$$

A set of reflecting planes matching these conditions is $(11\bar{1})$ and $(\bar{2}20)$. A final check is made by taking the cross-product $\vec{g}_1 \times \vec{g}_2 = [11\bar{1}] \times [\bar{2}20] = [224] \,||\, [112]$. We, therefore, assign the indices $g_1 = 11\bar{1}$, $g_2 = \bar{2}20$. All reciprocal lattice points on this section can be indexed using proper multiples of these two, e.g., $g_3 = g_1 + g_2 = \bar{1}3\bar{1}$, $g_4 = 2g_1 + g_2 = 04\bar{2}$,

$g_5 = g_1 - g_2 = 3\bar{1}\bar{1}$, etc. These are all normal to [112] and the resulting pattern is then completely indexed.

A similar proceedure can be used by comparing the ratios of the angles subtended by different sets of rel-vectors. Examples of calculated symmetrical spot patterns are given in several of the texts listed in the Bibliography at the end of this chapter.

Usually, in solving the diffraction pattern, it is not known what the normal to the pattern is, and the steps for solution are: (a) measure two rel-vectors, find their ratio and assign tentative $hk\ell$ values; (b) measure the angle between the two rel-vectors, assign signs and position indices such that the angle is correct; (c) cross the resulting rel-vectors and determine the zone axis of the reflecting planes; and (d) assign consistent indices to the rest of the spots on the pattern.

The distances measured on the diffraction pattern are actually magnified reciprocal lattice vectors; the magnification factor for the microscope is λL where L is the effective length resulting from the magnifications of the imaging lenses of the microscope column. That is, r, the distance on the diffraction pattern from the origin to a diffracted spot, is given by: $r = g(\lambda L)$, or $rd = \lambda L$. λL is called the camera constant from which d spacings for a crystal can be calculated.

Curvature of the Reflecting Sphere

That the reflecting sphere for high energy electrons is not completely flat can be illustrated using low magnifications of the front focal plane of the objective lens. For 100 kV electrons, the reflecting sphere intersects rel-points on the reciprocal layer containing the origin out to about 2 or 3 degrees so that many reflections appear within the zero

layer. At about 4 or 5 degrees it intersects points on the next higher rel-layer (or Laue zone) and at about 7 degrees, the third rel-layer. Thus, the reflecting sphere is not at all flat; but since the pattern is such a highly magnified view of a small section of reciprocal space, the approximation of a flat reflecting sphere is reasonable. As can be seen from the $(\lambda)^{-1}$ values of Table 1, the reflecing sphere becomes flatter the higher the accelerating voltage of the electrons.

4. THE SHAPE OF RECIPROCAL LATTICE POINTS

The Crystal Shape Factor

The intensity about the reciprocal lattice point has dimensions which are inversely proportional to the dimensions of the crystal. A spherical crystal would produce a spherical distribution of electrons about the rel-point. A disc-shaped specimen, which is roughly the shape of the irradiated part of the specimen in the electron microscope, would produce electrons distributed along a rod passing through the rel-point. These are called rel-rods and have their long axes normal to the thinnest direction of the crystal, i.e., along the axis of the microscope column. This phenomenon is simply a reflection of the fact that Bragg's Law is rigid only for a crystal of infinite dimensions. Relaxation of the law occurs for thin crystals and crystal planes can diffract waves at angles slightly different from the Bragg angle, although not as efficiently. The derivation of the intensity distribution due to this effect is given as follows.

Since the diffraction pattern is the Fourrier transform of the object, the intensities of diffracted beams depend on the shape and volume of the diffracting crystal. In specimens containing planar or volume defects

(e.g. small particles), two factors must be considered:

1. Shape factor due to the thinness of foils in the direction of the beam;

2. Shape factor due to the defects in the foil.

A useful physical picture of these effects is obtained by considering the diffraction pattern to be a composite formed by superposition of the diffraction patterns of the dispersed phases and the pattern of the matrix. If the structures are different, then, of course, the structure factors are also different and mixed reciprocal lattices must be considered.

The derivation of the shape factor can be accomplished by the kinematical theory of diffraction in which thin crystals and single scattering are assured. The approximations mean that strong Bragg diffraction does not occur i.e. that the reciprocal lattice point does not coincide with the reflecting sphere. Suppose the rel-point is at a distance s from the sphere {Fig 10(a)}.

The amplitude of the scattered wave is proportional to the atomic scattering amplitude times the phase factor summed over all atoms.

$$\Psi \sim \sum_{\text{atoms}} f_i \exp\left(2\pi i\, \bar{k}\cdot\bar{r}_i\right) \qquad (17)$$

Consider a parallel-piped crystal made up of unit cells each a x b x c in volume and N_1, N_2, N_3 are the number of unit cells scattering along the principal axes a, b, c. {Fig. 10(b)}

Let $\bar{r}$ = the position of atoms with respect to the origin of the crystal; $\bar{r}_n$ = the position of the unit cells with respect to the origin

of the crystal; $\vec{r}_i$ the position of an atom with respect to the origin of the unit cell and $\bar{k} = \bar{g} + \bar{s}$ {Fig. 10(a)}

$$\text{Thus } \Psi \sim \sum_{\text{atoms}} f_i \exp[2\pi i(g+s) \cdot (\bar{r}_i + \bar{r}_n)] \quad (18)$$

$$\sim \sum_{\text{all unit cells}} \left[\sum_{\text{all atoms per cell}} f_i [\exp 2\pi i\ (\bar{g} + \bar{s}) \cdot \bar{r}_i] \cdot \exp 2\pi i\ (\bar{g} + \bar{s}) \cdot \bar{r}_n \right] \quad (19)$$

now

$\sum_{\text{all atoms/cell}} f_i \exp 2\pi i\ (\bar{g} + \bar{s}) \cdot r_i$ does not depend on the shape of the crystal, and at $s = 0$, this becomes the structure factor F_g (Eq.10). Since $|s| << |g|$ the dependence on s is not very strong, hence

$$F_g \approx \sum f_i \exp [2\pi i(\bar{g} + \bar{s}) \cdot \bar{r}_i]$$

thus

$$\Psi \sim \sum_{\text{all unit cells}} F_g \exp [2\pi i\ \bar{g} \cdot \bar{r}_n] \exp [2\pi i\ \bar{s} \cdot \bar{r}_n] \quad (20)$$

Since $\bar{g} \cdot \bar{r}_n$ = integer, $\exp 2\pi i(\bar{g} \cdot \bar{r}_n) = 1$.

Also the quantity $\bar{s} \cdot \bar{r}_n$ does not change appreciably from cell to cell. Thus by approximating the sum by an integral

$$\Psi = F_g \int_{\text{crystal}} \frac{1}{V_c} \exp (2\pi i\ s \cdot r_n) \cdot dV \quad (21)$$

where V_c = volume of the crystal.

By definition $\bar{r}_n = u\bar{a} + v\bar{b} + w\bar{c}$

$$\bar{s} = s_x\bar{a}^* + s_y\bar{b}^* + s_z\bar{c}^*$$

$$\psi \cong \frac{F_g}{V_c} \int_0^{N_1 a} \int_0^{N_2 b} \int_0^{N_3 c} \exp\left(2\pi i(s_x x + s_y y + s_z z)\right) dx\, dy\, dz \quad (22)$$

which approximates to:

$$\psi \sim \frac{F_g}{V_c} \frac{\sin(\pi s_x N_1 a)}{(\pi s_x)} \frac{\sin(\pi s_y N_2 b)}{(\pi x_y)} \frac{\sin(\pi s_z N_3 c)}{(\pi s_z)}$$

which is known as the interference function.

For a crystal in the form of a thin plate $N_3 << N_2$, N_1 and for $s_x = s_y = 0$ (23)

$$\psi \sim \frac{F_g}{V_c} \frac{\mathrm{Sin}(\pi s_z N_3 c)}{(\pi s_z)} \quad (24)$$

$N_3 c = t$ the thickness of the plate, thus the intensity is

$$I \sim \left(\frac{F_g}{V_c}\right)^2 \frac{\sin^2(\pi t s_z)}{(\pi s_z)^2} \quad (25)$$

This well known function is shown in Fig. 11. It means that for thin foils in electron microscopy, the intensity distribution about the reciprocal lattice points is in the form of a rod. Likewise the shape transform (intensity distributions) for needles is in the form of discs (Fig. 12). These effects are very important in studies of precipitation; and two well known examples are the formation of small platelets of G. P. zones and θ" on {001} in Al-Cu and needles in <001> in Al-Mg-Si. Examples are shown in Fig. 13. Another example for microtwins is in Fig. 2(c).

The reciprocal lattice for the matrix as shown in Fig. 9 should thus be modified so that the "points" are rel-rods with the axis of the rods parallel to the incident beam as shown in Fig. 14a,b. If the crystal

is very thin, it is possible for rel-rods from the upper and lower levels of the reciprocal lattice to extend sufficiently to cut the reflecting sphere giving spots at positions which do not correspond to allowed reflections. In order to check for this effect, merely move into thicker parts of the foil when such spots will disappear.

Thus, sufficiently thin planar defects (twins, stacking faults or second phases) will give rise to rel-rods in the reciprocal lattice. The direction of the rel-rods is normal to the platelet since this is the direction along which the Laue condition is relaxed and, in the case of precipitation, in the early stages the rel-rods will pass through the matrix rel-points, i.e. the form factor dominates the diffraction pattern.

5. BEAM DIVERGENCE OR CONVERGENCE

A crystal may be oriented at the Bragg angle (for a certain set of planes) with respect to the optic axis of a diffraction unit but, unless the beam is perfectly parallel, the entire irradiated area will not be at the Bragg angle. For a divergent or convergent incident beam, there will be a continuous range of incident angles from one side of the Bragg angle to the other. The reciprocal lattice spot resulting from such an irradiated specimen will be spread out about the exact reciprocal lattice point. If the irradiated area is small, subsidiary maxima may occur on either side of the central maximum (exact Bragg condition) along the direction of the reciprocal lattice vector (Fig. 11). This represents periodic intensity oscillations in a foil of constant thickness with changing angle of incidence. In the image these produce fringes (s-fringes) at the reflecting positions called Bragg contours.

6. PRIMARY EXTINCTION

Another possibility is to have a constant angle of incident radiation on the specimen and observe the change in reciprocal lattice spot intensity distribution with changing foil thickness. In a completely analogous manner to the intensity oscillations with changing angle in a uniformly thick specimen, the intensity varies periodically with thickness at constant incident angle {for example, from Eq. 5, the kinematical intensity formula, whenever $s = n/t$ for constant t, or $t = n/s$ for constant s, we have intensity minima (Fig. 11)}. The kinematical theory predicts a central maximum at the Bragg angle for any thickness foil; actually, because of dynamical effects, there can be an intensity minimum surrounded by two maxima for certain thicknesses of foil. Thus the shape of the reciprocal lattice spot and the intensity distribution about the exact rel-point depends critically upon the thickness of the irradiated specimen. Although the rel-rods, due to small thickness, are still present, the distribution of intensity along the rel-rods can be vastly altered by changing the thickness by a relatively small amount. This is the phenomenon called primary extinction and gives rise to fringe contrast at inclined defects, holes, wedges etc.

7. INFORMATION FROM DIFFRACTION PATTERNS

The diffraction patterns provide basic crystallographic information such as the orientation of the specimens, orientation relationships between crystals, qualitative phase identification; and if Kikuchi patterns are utilized, geometrical structure factor analysis is possible as well as other information (see sec. 8). The diffraction pattern is the starting point for all electron microscopy; and in general, one of the

two orientation conditions shown in Fig. 14 are utilized.

The accuracy of analysis of a diffraction pattern depends upon accuracy of measurement and ~~are~~ is discussed in most of the books cited and in several publications (e.g. refs. 12-15). Some factors of importance are 1) the form factor as described above, which determines the shape of the intensity distribution about the rel-points and the relative orientation of the rel-rods to the reflecting sphere (Fig. 14a,b); 2) instrumental alignment and beam divergence (defocus the condenser lens to obtain as closely as possible parallel illumination); 3) specimen perfection (elastic and plastic strains); 4) curvature of the reflecting sphere and relative orientation of the foil; 5) double diffraction giving rise to reflections of zero structure factor.

Some further points should be made with regard to the interpretation of spot patterns viz.:

1) The assignment of directions is arbitrary; e.g. a four fold symmetrical pattern can be indexed in six possible ways 100, 010, 001 (and negatives). Thus the diffraction pattern of any crystal lying within the zero Laue zone (basal plane of the reciprocal lattice) will appear the same even if the crystal is rotated 180° about the incident beam so the orientation has changed.

2) For high index patterns some patterns of different zone axes are identical (e.g. $\bar{5}47$ and 815 fcc, $u^2 + v^2 + w^2 = 90$). Although one rarely works in high index orientations, the effect should be recognized.

It is impossible to cover all the various aspects of diffraction

patterns here, but the following examples are representative ones.

a) Double Diffraction

The Structure Factor determines that certain reciprocal lattice points, on an otherwise regular reciprocal lattice, have systematic absences i.e. zero intensity. It is necessary to determine these missing reflections to characterize the structure. However, each diffracted beam in the crystal behaves to some extent as an incident beam and can diffract electrons to a point on the diffraction pattern forbidden by the structure factor rules, especially in simultaneous orientations when several different reflections are excited. For example, the (002) reflection in the diamond cubic structure is not allowed, but if a [110] foil is viewed the reflection $(1\bar{1}1)$ acts as a primary beam, diffracting electrons from the $(\bar{1}11)$ planes, which gives $\vec{g}_1 + \vec{g}_2 = [1\bar{1}1] + [\bar{1}11] = [002]$. This is shown in Fig. 14(d). If the foil has [100] orientation, the two smallest reciprocal lattice vectors allowed are [022] and $[02\bar{2}]$, so that the (002) reflection cannot appear in this pattern. Similarly, the (0001) reflection in HCP crystals, which is not allowed, arises through the combination of two reciprocal lattice vectors such as in the $[11\bar{2}0]$ orientation $\vec{g}_1 + \vec{g}_2 = [0\bar{1}10] + [01\bar{1}1] = [0001]$ and in $[\bar{1}2\bar{1}3]$, $[\bar{1}101] + [\bar{1}010] = [\bar{2}111]$. This phenomenon of rediffracting a diffracted beam is very common and is called double diffraction. Although it is sometimes difficult to avoid these effects, tilting the foil so as to remove one of the diffracted beams which is required for the double diffraction will remove the forbidden reflection e.g. Fig. 14(c). This effect is very important in multiphase alloys and can lead to erroneous identification of phases (e.g. ref. 16).

It should be noted that in fcc or bcc crystals, double diffraction does not introduce extra spots since the combination of any two diffracted beams generates only allowed reflections. For example for bcc $110 \pm 200 \rightarrow 310$ or $\bar{1}10$. Although no extra spots will be observed, double diffraction will obviously increase the intensity of those spots where superposition occurs. However, double diffraction in twinned fcc or bcc crystals can introduce extra spots.

b) Moiré Patterns

A special case of double diffraction occurs from overlapping crystals such as in composite films, or in two (or more) phase systems. Two general cases occur. Firstly, parallel moirés which are formed from parallel reflecting planes of different spacings corresponding to reciprocal lattice vectors $\vec{g}_1 \vec{g}_2$ differing only in magnitude. In practice it may be difficult to resolve two separate rel-points if g_1 and g_2 are almost equal. The effective reciprocal lattice vector for the composite is thus $\vec{g}_1 - \vec{g}_2$ (for $\vec{g}_1 > \vec{g}_2$) corresponding to a moire image spacing $D_p = (g_1 - g_2)^{-1}$ and lying normal to $\vec{g}_1$, $\vec{g}_2$. An example for a Cu-Mn-Al alloy containing coherent phases utilizing 111, 222, and 333 reflections is shown in Fig. 15. It can be seen that D_p varies inversely as Δg.

Secondly, the rotational moiré is formed when planes of equal spacing d, but mutually rotated through an angle α, diffract together. In this case, the effective reciprocal lattice vector is $g \sin\alpha$ and the moiré image spacing D_r is $(g \sin\alpha)^{-1}$ i.e. d/α). Mixed moirés can occur due to two overlapping gratings of different spacings and which are relatively twisted by a small angle.

c) Faulted Crystals

Since in electron diffraction it is possible to consider diffraction from a narrow column of crystal, then even for a single intrinsic stacking fault, where four layers are in HCP stacking: ABCAB ⋮ CACA ⋮ BCA, there may be a sufficient volume of HCP material present so that the layers can be regarded as a thin platelet of HCP structure. One can then consider the diffraction pattern from a foil containing a fault in terms of two reciprocal lattices, viz., one "normal" pattern corresponding to the matrix and the other consisting of the streaked HCP reciprocal lattice, corresponding to the thin fault, superimposed. (13) Since the fault plane is one of the four $\{111\}$ in FCC and because of the unique crystallographic relations between FCC and HCP lattices, the rel-rods will lie along <0001> hcp parallel to and coincident with <111> fcc continously throughout reciprocal space. These streaks which can be considered to originate from HCP reciprocal lattice points will thus pass through all matrix reflections contained in the particular [111] and parallel zones. Examples for $[\bar{1}01]$ and [112] orientations are sketched in Fig. 16(a,b). In support of this view, consider a diffraction pattern taken from a single fault lying parallel to the incident beam (Fig. 16a). Fig. 17 illustrates such a case for growth faults in silicon. The foil is oriented with $[\bar{1}01]$ parallel to the incident beam and the "edge-on" faults on (111) and $(\bar{1}1\bar{1})$ are joined by a fault on $(11\bar{1})$ or $(\bar{1}11)$ inclined at 35° to the beam. By placing a small field limiting aperture over the edge-on fault at A, the diffraction pattern in Fig. 17(b) was obtained. It can be seen that streaks are visible along [111] and pass through (000) and the other rel-points. These streaks can be attributed to the stacking

fault acting as a thin (HCP) platelet; the structure is indeterminate in the direction of streaking, as no maxima are visible along [111]. If a larger fraction of edge-on faults were to contribute to the pattern; or if there were regular faulting on alternate (111) planes over a sufficient volume of crystal, then the $[\bar{1}01]$ pattern would contain resolvable HCP maxima as sketched in Fig. 16(a).

Fig. 17(c) is a diffraction pattern taken across the inclined fault B shown in Fig. 17(a) after the foil was tilted into a strong 202 beam case (i.e. the reflecting sphere passed exactly through the 202 rel-point). Doublets (arrowed) can be resolved in the pattern. These doublets are due to both the effects of matrix and fault rel-rods. The orientation of Fig. 17(c) is then almost exactly $[\bar{3}\bar{1}3]$ and this may also be taken as the normal to the foil surface. There are two possible streaking directions depending on whether the fault is on $(\bar{1}11)$ or $(11\bar{1})$. By suitable projection, it can easily be shown that the spots to the inside of the doublets can only arise from streaks due to a $(11\bar{1})$ fault. The positions of these inner spots are exactly where the $[11\bar{1}]$ streaks are expected to cut the reflecting sphere for this orientation. The outer spots of the doublets arise from foil thickness rel-rods and their distance from the inner spots corresponds to that calculated for rel-rods along $[\bar{3}\bar{1}3]$. This example serves to emphasize the importance of precise orientation determinations for explaining fine detail in diffraction patterns.

d. Twin Patterns

Twinning is a phenomenon commonly observed as a result of plastic deformation as well as occurring during martensitic and bainitic phase transformation (e.g., in ferrous alloys and steels), and is of considerable importance in controlling mechanical properties as will be discussed

in a later chapter. The analysis of twinned diffraction patterns is facilitated with the aid of stereographic projection, or by calculation using matrix algebra; together with dark field microscopy. (refs. 17-19)

A twin is obtained by shear such that all atomic sites on one side of the twin boundary are in mirror image relationship to those on the other. For fcc and bcc crystals the twin planes are $\{111\}$ and $\{112\}$ respectively. An alternative description of twinning is that of 180° rotation about the twin plane normal (twin axis). These relationships enable the matrix of the transformation to be readily derived. Since the indices of reciprocal lattice points are the Miller indices of the diffracting planes, the reciprocal lattice for the twinned crystal will be related to that of the original crystal by the twinning matrix. The indices of a reciprocal lattice point [PQR] for the twinned crystal will be related to the point [pqr] in the reciprocal lattice of the original crystal after twinning on the (hkℓ) plane {rotation of 180° about the normal to (hkℓ)} by the following general expression:

$$P = \frac{p(h^2 - k^2 - \ell^2) + q(2hk) + r(2h\ell)}{h^2 + k^2 + \ell^2} \tag{26}$$

$$Q = \frac{p(2hk) + q(-h^2 + k^2 - \ell^2) + r(2k\ell)}{h^2 + k^2 + \ell^2} \tag{27}$$

$$R = \frac{p(2h\ell) + q(2k\ell) + r(-h^2 - k^2 + \ell^2)}{h^2 + k^2 + \ell^2} \tag{28}$$

In matrix form, this can be written $(PQR) = T_{hk\ell} \cdot (pqr)$.

Therefore, the general twinning matrix for the cubic system is:

$$T_{(hk\ell)} = \frac{1}{h^2+k^2+\ell^2} \begin{pmatrix} h^2-k^2-\ell^2 & 2hk & 2h\ell \\ 2hk & -h^2+k^2-\ell^2 & 2k\ell \\ 2h\ell & 2k\ell & -h^2-k^2+\ell^2 \end{pmatrix} \tag{29}$$

The indices for reflection in the twin plane are obtained by multiplication of this matrix by $\begin{vmatrix} \bar{1}00 \\ 0\bar{1}0 \\ 00\bar{1} \end{vmatrix}$

i.e. the indices are PQR after rotation, but are $\bar{P}\bar{Q}\bar{R}$ after reflection. (The reader can prove this using Fig. 8).

In the fcc systems twinning occurs on {111} planes and so in general:

$$T = \frac{1}{3}\begin{pmatrix} -1 & 2hk & 2h\ell \\ 2hk & -1 & 2k\ell \\ 2h\ell & 2k\ell & -1 \end{pmatrix} \quad \text{e.g. for } T = (111) = \frac{1}{3}\begin{pmatrix} -1 & 2 & 2 \\ 2 & -1 & 2 \\ 2 & 2 & -1 \end{pmatrix}$$

In bcc materials twinning occurs on {112} planes, hence:

$$T_{\{112\}} = \frac{1}{3}\begin{pmatrix} \frac{h^2-k^2-\ell^2}{2} & hk & h\ell \\ hk & \frac{-h^2+k^2-\ell^2}{2} & k\ell \\ h\ell & k\ell & \frac{-h^2-k^2+\ell^2}{2} \end{pmatrix}$$

The appropriate twin plane indices can be substituted for each case. (e.g. Table 4). For either fcc or bcc twinning the elements inside the matrices shown are integers. Then, because of the factor 1/3 outside the matrix, all third order reciprocal lattice spots for the matrix will coincide with allowed reciprocal lattice spots for the twin. Table 4 illustrates for the third order of the two shortest reciprocal lattice vectors in each system, the twin reciprocal lattice points obtained by transformation of the original reciprocal lattice points, i.e., in a diffraction pattern from both crystals, these diffracted spots would coincide. (as is plotted in Fig. 16(a). It should be noted that if the twinned region is very narrow, the twin reciprocal lattice will be streaked along <111>. Fig. 2(c) shows such streaks corresponding to the microtwins spaced ≈ 20Å shown in Fig. 2(b).

Notice also that twin C is faulted.

Table 4

Twin Indices PQR of Matrix Reflections pqr for the First Two Sets of Allowed Reflections in fcc and bcc Crystals*

FCC		BCC	
pqr	PQR [(hkℓ) = (111)]		PQR [(hkℓ) = (112)]
333	$\bar{3}\bar{3}\bar{3}$	330	$\bar{1}\bar{1}4$
$33\bar{3}$	$\bar{1}\bar{1}5$	303	033
$3\bar{3}3$	$\bar{1}5\bar{1}$	033	303
$\bar{3}33$	$5\bar{1}\bar{1}$	$\bar{3}30$	$3\bar{3}0$
600	$\bar{2}44$	$30\bar{3}$	$4\bar{1}1$
060	$4\bar{2}4$	$03\bar{3}$	$\bar{1}4\bar{1}$
006	$44\bar{2}$	600	$\bar{4}24$
		060	$2\bar{4}4$
		006	442

*The indices are obtained by the rotation matrix. For reflection (as in stereograms) the PQR indices are the negatives of those shown.

Reflections of different indices coincide when the sum of the squares of their indices are the same since then the Bragg angles are also the same. Thus {333} and {511} coincide in fcc patterns ($h^2 + k^2 + \ell^2 = 27$) and {411} and {330} in bcc patterns, ($h^2 + k^2 + \ell^2 = 18$). Notice that if a 511 fcc matrix spot twins to 333, then 222 twin and 111 twin spots also appear in the pattern. Such a case exists with <105> orientations; and an example for double twinning in shock loaded copper is given in Fig. 18. This example also illustrates how dark field imaging enables twin spots to be identified. The interpretation by stereographic projection is shown in Fig. 19. Fig. 20 shows another example of (112) twinning in Fe-Ni martensite (bcc) in which extra spots from double diffraction also occur (20). Fig. 2(b) shows direct lattice images of twins in silicon.

In fcc crystals, it can be seen that twin spots either coincide with matrix spots or are positioned 1/3 along <111> directions. For example, in fcc with twin plane (hkℓ)

$$(\bar{1}11) \rightarrow \frac{1}{3}(5\bar{1}\bar{1})_T = 200 - \frac{1}{3}(111)$$

$$200 \rightarrow \frac{1}{3}(\bar{2}44)_T = \bar{1}11 + \frac{1}{3}(111)$$

$$\bar{2}44 \rightarrow (600)_T; \text{ see also Table 4.}$$

The twin points that do not coincide with matrix points are thus displaced from matrix points by vectors of ± 1/3 <111>. However, not all of the one-third points are occupied as can be shown from the following. The twin points $u_1v_1w_1$ of matrix points uvw are $u_1 = (u \pm \frac{1}{3}h)$, $v_1 = (v \pm \frac{1}{3}k)$, $w_1 = (w \pm \frac{1}{3}\ell)$. Remembering the structure factor rule for fcc crystals ($h_1k_1\ell_1$ or $u_1v_1w_1$ must be all odd or all even), and that $\vec{g}$ (uvw) must equal $\vec{g}_1$ $(u_1v_1w_1)$, then

$$(u_1^2 + v_1^2 + w_1^2) - (u^2 + v^2 + w^2) = 4N \qquad (32)$$

where N = integer for $u_1v_1w_1$, u v w , both all even or both all odd.

also $$(u_1^2 + v_1^2 + w_1^2) - (u^2 + v^2 + w^2) = 2N + 1 \qquad (33)$$

for $u_1v_1w_1$ all even, u v w all odd, or vice-versa. Hence, if uvw are all even, the twin point $u_1v_1w_1$ must have all odd indices and vice-versa. It, therefore, follows that the allowed twin points $(u \pm \frac{1}{3}h)$; $(v \pm \frac{1}{3}k)$,

$(w \pm \frac{1}{3}\ell)$ for the 2N + 1 condition is given by the following selection rule:

$$hu + kv + \ell w = (3N + 1) \qquad (34)$$

This rule determines whether a point $(u \pm \frac{1}{3}h)$, $(v \pm \frac{1}{3}k)$, $(w \pm \frac{1}{3}\ell)$ is occupied by a twin spot. Similar arguments apply to bcc and hcp lattices and is discussed in detail in references 17 and 18.

The stereographic projection is also convenient for analysing twinning (ref. 19). The twin plane great circle is drawn and reflections which will appear in the diffraction pattern due to twinning will be those which after reflection fall on the basic circle. This is illustrated in Fig. 8 for (111) twinning in the [001] fcc orientation, and in Fig. 19 for double twinning on $(1\bar{1}\bar{1})$ and $(1\bar{1}1)$ in the $[5\bar{1}0]$ fcc orientation. The required poles are those which lie at an equal angle to the twin plane as the twin plane is from the basic circle. These poles, thus, also lie on a great circle. This is shown in Fig. 8 as the dotted circle for (111) twinning, and demonstrates how the $\bar{2}\bar{4}0$ matrix reflection coincides with the 204 twin spot. As an exercise, the reader can show that the twin orientation is $\bar{2}\bar{2}1$, and that no extra spots appear in the pattern.

e. Sidebands - Modulated Structures

Another important effect arises when periodic modulations, wavelength λ_p in composition occur, such as in spinodal alloys. Such modulations produce modulations in lattice parameter. The period of modulation appears in the diffraction pattern as side-bands (21,22) whose spacing is inversely proportional to λ_p. Examples are shown in Fig. 21.

For cubic crystals, the periodic wavelength is given by:

$$\lambda_p = \frac{a_0 h}{(h^2+k^2+\ell^2)} \cdot \frac{\tan\theta}{\Delta\theta} \qquad (35)$$

where uvw is the direction of fluctuation (001 for Fig. 21) and $\Delta\theta$ the angular separation between a main spot and its sideband spot. In the diffraction pattern, the corresponding sideband spacing is Δ_p. Since θ is small, for (h00) reflections, we obtain (22):

$$\lambda_p = \frac{ha}{(h^2+k^2+\ell^2)} \cdot \left(\frac{g}{\Delta_p}\right) \qquad (36)$$

where $g/\Delta p$ is obtained directly from the pattern. Examination of (36) shows that Δp is independent of $\bar{g}$, i.e. the order of reflections. The values are also independent of microscope magnification.

For accurate measurements, choose orientations such that the diffraction pattern contains the direction(s) of modulation; otherwise Δp is projected.

The direction of Δp is parallel to the direction of the modulation {generally <001> in cubic systems} whereas Δg, the difference in lattice parameter between the two phases is parallel to $\vec{g}$. Thus, the spacing of the doubling of spots due to the two different lattice spacings increases with increasing g for all spots, radially outwards from the origin. As shown in Fig. 15, this effect produces Moiré fringes of smaller spacing as Δg increases with $\vec{g}$. Consequently, it is easy to distinguish sidebands (due to periodic fluctuations in composition) from doubling of reflections (due to differences in lattice parameter) just by observation of the diffraction pattern out to several orders.

An example of sidebands from a modulated ordered alloy of $Cu_{2.5}Mn_{0.5}Al$ is shown in Fig. 21(d). They are well resolved in the central superlattice spots. The modulations are shown in the images of Fig. 21(a-c), and faint antiphase domain boundaries are also visible. {Chapter 2, Sec 8(d)}.

f. Mixed Patterns - Identification of Phases

If n orientations or phases in a specimen contribute to a diffraction pattern, n spot patterns will appear and each pattern can be individually indexed. Although in certain cases of matching such as twinning, superposition of patterns can occur. Dark field imaging will generally allow this to be recognized.

Supposing a foil contains a second phase which is large enough to produce an identifiable pattern. The second phase can be identified by calibration of the pattern using the matrix spots. To avoid difficulties from rel-rod projections and to obtain the most accurate measurements, the foil should be oriented to give a symmetrical diffraction pattern {Fig. 14(b)}.

As an illustration, consider Fig. 22, which is a pattern from a quenched and tempered Fe-Ni-C alloy, containing carbide particles in addition to the BCC α matrix. The matrix spots are indexed as shown. They are in $[\bar{1}01]$ orientation. From the measured r values on the pattern and taking a_0 for Bcc Fe as 2.861Å, an average value of the camera constant $\lambda L = 2$Å cm is obtained by plotting r versus $\left\{h^2 + k^2 + \ell^2\right\}^{\frac{1}{2}}$ since the slope of this plot is $\lambda L/a$.

The spots of lower intensity correspond to carbide reflections. Their d-spacings are $\lambda L/r_c$ where r_c are distances of carbide spots from the origin. The d-values so obtained are listed in Table 5. By comparison of these d values with those listed in the ASTM card index file, it can be seen that the carbide is cementite, which is orthorhombic. These spots may now be indexed as shown in Fig. 22. The cementite spots give a single crystal pattern in [100]. It can be seen that the cementite pattern is crystallographically oriented with respect to the α-BCC pattern. It follows that the orientation relationships are: $[\bar{1}01]_\alpha \| [100]_c$, $[\bar{1}2\bar{1}]_\alpha \| [001]_c$, $[111]_\alpha \| [010]_c$.

TABLE 5

Some d-spacings from Fig. 22 as measured on the original negative

Distance of Spots from Origin r (cm)	d = λL/r	Reflection (Compared to ASTM Card #6-0688 for Fe_3C Reflections
0.59	3.39	002
1.18	1.69	004
0.83	2.5	020
1.66	1.25	040

g. Ring Patterns

For a randomly oriented set of crystalline grains, diffraction produces a series of cones, each cone of angle 4θ where θ is the Bragg angle for the particular reflection. These cones intersect the reflecting sphere on a circle; and as in a spot pattern, the radius of the circle r is given by $\lambda L/d$. This is true for all crystals. The breadth and spottiness of the ring pattern depends on the size and number of crystals contributing to the pattern as shown in Fig. 23. The finer the grain size, the broader is the pattern; and there is a lower limit beyond which the physical definition of "crystalline" grains becomes difficult. Thus in some cases, very diffuse broad ring patterns may be referred to as originating from "amorphous" solids, whereas in fact, the material may be crystalline, but only a few unit cells in grain size. Thus, great care must be exercised in drawing conclusions about the nature of the material merely from the breadth of the pattern, even if dark field images are also obtained of the individual crystals (Fig. 23). In such cases, lattice imaging techniques should be utilized, as discussed in a later chapter by Dr. Howie. These considerations are particularly important in thin films e.g. in applications of the so called "amorphous" solids which have useful properties as semiconductors and superconductors.

Ring patterns can be useful for qualitative identification of materials; their analysis is similar to that for x-ray powder patterns. The main difference is that in electron diffraction, we are in the region $\sin 2\theta \simeq 2\theta$. If the camera constant λL is known, then d-values can be calculated from the relation $\lambda L = rd$. One way of fixing λL is to evaporate a known material such as gold, onto part of the specimen being investigated.

This pattern can be superimposed on the unknown by doubly exposing the plate or film. Then λL can be evaluated from the gold pattern e.g. by plotting the ring radii which will appear in the sequence $\{111\}$, $\{200\}$, $\{220\}$, $\{311\}$ etc. (Table 3) against $\sqrt{h^2+k^2+\ell^2}$ and finding the slope. Since a_0 for gold is known λL is found. The unknown d values are then found by dividing λL by the measured radii from rings of the unknown substance, and using the ASTM card index file.

Considerable care must be exercised in such work. For example, if the grain structure is not perfectly random, not all reflections will appear. Suppose, for example, a fcc polycrystal had a [001] preferred fibre orientation. Then reflections for which $[001]\cdot[hk\ell] \neq 0$ would not appear. Hence 111, 311 rings would be absent. Also the structure of thin films may not necessarily be the same as that of the bulk, expecially if produced under non-equilibrium conditions (such as very fast rates of evaporation or "splat" cooling). For example, the tin patterns of Fig. 23 do not conform to the normal tetragonal sequence of reflections. Double diffraction may also cause the appearance of "forbidden" reflections.

8. KIKUCHI PATTERNS

As the thickness of a specimen is increased, Kikuchi line patterns are observed in addition to spots; with further increase in thickness, only Kikuchi patterns will be observed until eventually no coherent diffraction will occur because of complete absorption is very thick specimens.

Kikuchi patterns are produced only in relatively thick and perfect crystals. They are formed as a result of Bragg scattering of the inelastic electrons and appear as pairs of parallel lines in the diffraction image (Fig. 24). They lie normal to the particular $\vec{g}$, and are related to the

spot pattern as shown in Fig 14. The pairs of Kikuchi lines always subtend an angle of exactly 2θ, irrespective of the foil position; and their separation is thus always an exact, but magnified, measure of g. Since more electrons are scattered in the forward direction, then on a positive print a bright line will be present near a reciprocal lattice point and a corresponding dark line near the origin (000). For the symmetrical orientation, the two lines have about equal intensity.

For electron microscopy, there are two important orientations of the specimen: 1) systematic Bragg reflection, and 2) symmetrical orientation. The former is a prerequisite for contrast work and the latter for orientation determinations. Both are easily achieved if a goniometric tilt specimen holder is used. As can be seen from Fig. 14, these two positions are related simply by a tilt of θ° if in a) the first order Bragg reflection is excited. The position of the Kikuchi line, with respect to the spot pattern, determines the exact relationship between the diffracting planes in the crystal and the direction of the incident beam. Thus, it is possible to obtain the orientation of a foil to better than 0.1°, which is more accurate than by the x-ray Laue method. Also, the position of the Kikuchi pattern relative to the spot pattern determines the sign and magnitude of s and gives the direction and tilt of the specimen with respect to the beam. The tilt angles can thus be calibrated by measurements of Kikuchi line shifts. For an electron microscope with $\lambda L \simeq 2\text{Å}$ cm a tilt of 1° of the foil corresponds to a shift of Kikuchi lines of about 1 cm on the plate.

The Kikuchi lines can be easily indexed from the symmetry of the patterns or from measurements of their widths since the latter are related

to the d-spacings through the camera constant equation,

$$\lambda L = p_1 d_1 = p_2 d_2 = p_n d_n$$

$$\frac{p_1}{p_2} = \frac{d_2}{d_1}$$

where p_1, etc., is the width of a parallel hkℓ Kikuchi pair corresponding to a spacing d (hkℓ). Therefore, the ratios of the spacings enable the lines to be indexed just as for a spot pattern. For cubic crystals, Table 3 can be used.

As can be seen from Fig. 24, the center of the Kikuchi pair is the trace of the reflecting plane in the diffraction pattern and these must make the precise angles to each other as required by the crystallographic relations for the particular crystal. The indexing is thus easily checked by measuring these angles.

Indexing and orientation analysis is greatly facilitated by the use of Kikuchi maps as described in great detail elsewhere (see Ref. 22 for review). An example for hcp crystals which is indexed in the Miller-Bravais notation for directions so as to apply to all hcp systems is given in Fig. 25. Orientations are identified by comparing the unknown pattern to the relevant map.

Because orientations can be determined very accurately, one of the most obvious advantages of using Kikuchi patterns is in determining orientation relationships, misorientations due to sub-boundaries, and

other detailed crystallographic information. (12,13,23,24)

The following summarizes some of the applications of Kikuchi patterns:

1) Precise determination of foil orientations, and orientation relationships.
2) Calibration of rotation with magnification change.
3) Calibration of tilting stages.
4) Calibration of wavelength (and voltage).
5) Measurement of lattice spacings.
6) Identification of phase changes.
7) Facilitates contrast analyses - selection of appropriate diffraction conditions. (See Chapter 2)
8) Measuring internal strains in crystals.

These have been discussed and reviewed in some detail, and the reader is referred to references 12, 23, 24 for this information.

ACKNOWLEDGEMENTS

These two chapters are abstracted from a book on electron microscopy in preparation by Dr. W. L. Bell and myself.

Most of the illustrations used are taken from our own research programs and I acknowledge continued financial support of the United States Atomic Energy Commission through the Inorganic Materials Research Division of the Lawrence Berkeley Laboratory. I am grateful to several past and present members of my group and to Dr. V. A. Phillips for permission to use unpublished results. These are indicated in the pertinent figure captions.

A REPRESENTATIVE GENERAL BIBLIOGRAPHY FOR TRANSMISSION ELECTRON MICROSCOPY

CHAPTERS 1 and 2

Transmission Electron Microscopy of Metals, G. Thomas, J. Wiley and Sons, N.Y., 1962.

Electron Microscopy of Thin Crystals, P. B. Hirsch, A. Howie, R. B. Nicholson, D. W. Pashley and M. J. Whelan, Butterworths, 1965.

Techniques for Electron Microscopy, D. H. Kay, Ed., Blackwell Sci. Pubs., 1965.

Thin Films, Amer. Soc. Metals, (Chaps 3, 8-10), 1964.

Fundamentals of Transmission Electron Microscopy, R. D. Heidenreich, Wiley-Interscience, N.Y., 1964.

Modern Diffraction and Imaging Techniques in Materials Science, Eds. S. Amelinckx et al., North Holland Press, 1970.

Modern Metallographic Techniques and Their Application, V. A. Phillips, Wiley-Interscience, 1971.

Electron Microscopy in Materials Science, U. Valdre, Ed., Academic Press, N.Y., 1971.

Einführung in die Elektronenmikroskopie, M. von Heimendahl, F. Vieweg, Braunschweig, 1970.

Durchstrahlungs - Elektronenmikroskopie Fester Stoffe, E. Hornbogen, Verlag Chemie, Weinheim, 1971.

Interpretation of Electron Diffraction Patterns, K. W. Andrews, D. J. Dyson and S. R. Keown, Hilger and Watts, London, 1967.

Electron Microscopy and Strength of Crystals, Eds. G. Thomas and J. Washburn, Wiley-Interscience, 1963.

Electron Microscopy and Structure of Materials, Ed. G. Thomas, Univ. Calif. Press, 1972.

Electron Optics and Electron Microscopy, P. W. Hawkes, Taylor and Francis Ltd. (London), 1972.

Stereographic Projection and Applications, O. Johari and G. Thomas, Wiley-Interscience, 1969.

Crystallography and Crystal Defects, A. Kelly and G. W. Groves, Longman, 1970.

References Chapter 1

1. Dupouy, G., Adv. Opt. Electron Microsc., 2, 167 (1968).
2. Cosslett, V. E., Modern Diffraction and Imaging Techniques in Materials Science, Eds. S. Amelinckx et al. North Holland Press, 341 (1970).
3. Howie, A., ibid 295.
4. Bell, W. L. and Thomas, G., Electron Microscopy and Structure of Materials, Ed. G. Thomas, Univ. Calif. Press, 23 (1972).
5. Fisher, R. M., ibid 60.
6. Fisher, R. M., Proc. 26th EMSA Meeting, Claitors Publishers La., 324, (1968).
7. Humphries, C. J., Phil. Mag, 25, 1459 (1972).
8. Menter, J. W., Adv. Phys., 7, 299 (1958).
9. Komoda, T., Jap. J. Appl. Phys., 5, 603 (1966).
10. Phillips, V. A., Modern Metallographic Techniques and Their Applications, Wiley-Interscience (N.Y.), 256-272 (1971).
11. Allpress, J. G. and Sanders, J. V., Electron Microscopy and Structure of Materials, Ed. G. Thomas, Univ. of Calif. Press, 134 (1972).
12. Okamoto, P. R. and G. Thomas, Phys. Stat. Sol., 25, 81 (1968).
13. Thomas, G., Bell, W. L. and Otte, H.M. Phys. Stat. Sol, 12, 353 (1965).
14. Ryder, P. L. and Pitsch, W., Phil. Mag., 18, 807 (1968).
15. Samudra, A. V., Johari, O. and Heimendahl, M. V., Practical Metallography, 9, 516 (1972).
16. Thomas, G., Cheng, I-Lin and Mihalisin, J. R., Trans. ASM, 62, 852 (1969).
17. Pashley, D. W. and Stowell, M. J., Phil. Mag., 8, 1605 (1963).
18. Bullough, R. and Wayman, M., Trans. AIME, 236, 1704 (1966).
19. Johari, O. and Thomas, G., Stereographic Projection and Applications, Wiley-Interscience (N.Y.) (1969).

20. Thomas, G. and Das, S. K., J. Iron Steel Inst., 209, 801 (1971).

21. Daniel, V. and Lipson, H., Proc. Roy. Soc., A182, 378 (1943).

22. Butler, E. P. and Thomas, G., Acta Met., 18, 347 (1970).

23. Thomas, G., Modern Diffraction and Imaging Techniques in Materials Science, Eds. S. Amelinckx et al., N. Holland, 159 (1970).

24. Thomas, G., Trans. AIME, 233, 1608 (1965).

CHAPTER 1 FIGURE CAPTIONS

Fig. 1. Scheme showing the functions of transmission electron microscopy (ref. 23, Courtesy N. Holland Publishers).

Fig. 2(a). Phase contrast imaging from a periodic object. The diffraction pattern is formed in the back focal plane. The period d is imaged as magnified fringes if the diffracted and transmitted beams recombine at the image plane (when $2\theta < \alpha$) (see b). Notice the inversion between diffraction pattern and image relative to the object. (b) {111} lattice fringes obtained by tilted illumination showing microtwins A,B,C,D in silicon. Notice twin C contains a stacking fault. (c) Selected area diffraction pattern 011 (matrix) of area in (b) showing position of 30μ aperture which includes matrix and twin reflections. Notice streaks in $[1\bar{1}1]$ due to microtwins. (b,c courtesy V. A. Phillips, Acta Met., 20, 1143 (1972).

Fig. 3. Amplitude contrast imaging: the phases of the transmitted and diffracted beams do not recombine. Objective apertures are used to stop off the diffracted beams to form a bright field image (a). Dark field images are obtained by gun tilting or beam deflection (b) or with an off-axis aperture (c).

Fig. 4. Examples of bright and dark field images from faults in fcc cobalt. Notice the poor resolution in the off-axis aperture dark field image (c), compare to Fig. 3 (ref. 24 Courtesy AIME).

Fig. 5. Properties of electrons as a function of voltage, relative to those at 100 kV (after Fisher ref. 6).

Fig. 6. Experimental data on penetration in silicon and stainless steel (Lacaze and Thomas, J. Mic. in press 1973).

Fig. 7. Bragg's Law and the reflecting sphere for fast electrons.

Fig. 8. Standard cubic [001] stereographic projection showing great circles for poles 90° from 111 and $0\bar{1}3$ respectively. The dotted circle contains poles which will twin by reflection to the basic 001 circle for (111) twinning.

Fig. 9. The reciprocal lattice: for cubic crystals a = b = c and the corresponding reciprocal lattice points for diffraction for fcc and bcc crystals are shown.

Fig. 10(a). Showing relation between the reciprocal lattice and reflecting sphere when Bragg's Law is not exactly satisfied. (b) Sketch of a column of unit cells in a parallelpiped crystal for calculating the interference function.

Fig. 11. The interference function along S_z direction showing the kinematical intensity distribution for this foils.

Fig. 12. Interference functions for crystals of small sizes showing the effect of the shape factor on the diffraction pattern. (i) thin plates normal to the beam (ii) parallel to the beam (iii) needles parallel to the (iv) inclined to the beam. Notice curved streaks in (iv) (compare to Fig. 13).

Fig. 13(a). Dark field image of needles in <001> in an aged Al-Mg_2Si alloy (b) interference function for the three (001) needles (c) 011 diffraction pattern showing curved streaks for needles along [001] and [010] at 45° to beam (cf. Fig. 12(iv) (d) [011] diffraction pattern for Al-Cu containing thin plates (of G.P. zones) on <001>; notice straight streaks in [100] from (100) plates (cf. Fig. 12(ii).

Fig. 14. Diffraction geometry for thin foils (a) oriented for 2 beam excitation (b) symmetric orientation. For thick foils, Kikuchi lines will also appear as shown. (c,d) are spot patterns from silicon corresponding to a,b: notice the appearance of the forbidden 200 spots in the 011 pattern in (d) due to double diffraction (absent in c). (a,b ref. 13 courtesy Phys. Stat. Sol.).

Fig. 15. Parallel moiré patterns in aged Cu-Mn-Al alloy. Notice how the spacing varies inversely as Δg for the 111, 222 and 333 reflections. (courtesy M. Bouchard).

Fig. 16(a). Calculated $[\bar{1}01]$ pattern for a fcc crystal containing thin faults or hcp precipitates (with ideal c/a ratio) on (111). Twin spots are also shown. (b) As (a) but for a [112] foil containing faults or precipitates on all four {111} showing the effect of rel-rods on the diffraction pattern.

Fig. 17. Stacking faults in silicon (a) bright field image, foil near $[10\bar{1}]$ (b) diffraction pattern from region A {compare to 16(a)} (c) diffraction pattern (after tilting) corresponding to region of inclined faults B {compare to 16(b)} (Ref. 13 courtesy Phys. Stat. Sol.).

Fig. 18. Twins in copper as a result of explosive deformation (a) bright field image (b) diffraction pattern indexed (c,d) dark field images using the different twin spots from T_1, T_2 showing contrast reversal of twins. {Courtesy Acta Met., 12, 1153 (1964)}.

Fig. 19. Stereographic projection corresponding to Fig. 18 showing the twin planes must be $(1\bar{1}\bar{1})$ and $(1\bar{1}1)$. {Courtesy Acta Met., 12, 1153 (1964)}.

Fig. 20(a). Bright field image (b) Diffraction pattern showing {112} transformation twinning in Fe-32% Ni martensite. The $\bar{1}\bar{1}3$ primary twin spot pattern superposes on [113] matrix; double diffraction spots are arrowed. Primary twin plane is $(21\bar{1})_\alpha$ (c,d) are dark field images of $(110)_T$ and $(1\bar{1}0)$ matrix respectively. (Ref. 20 courtesy J. Iron and Steel Inst.).

Fig. 21(a,b,c) Bright field images of spinodal microstructure of $Cu_{2.2}Mn_{0.8}Al$ showing coarsening of the wavelength with aging at 350°C for (a) 30 sec. (b) 1 min. (c) 2 min. 220 fundamental reflection. (Courtesy M. Bouchard). (d) Diffraction patterns of 200 superlattice and 400 fundamental spots showing sidebands in <100> corresponding to modulations shown in a,b,c after aging at 200°C for times shown in minutes. Structure corresponds to L21 superlattice. (Courtesy M. Bouchard).

Fig. 22. Diffraction pattern of a tempered 0.3% carbon steel showing the [100] orthorhombic (Fe_3c) pattern superposed on the $[\bar{1}01]$ bcc pattern. (Courtesy O. Johari).

Fig. 23. Dark field images and ring patterns from vacuum evaporated tin showing change in grain size. Arcing of rings indicates preferred orientation. (Courtesy W. L. Bell).

Fig. 24. Sketches showing origin of Kikuchi lines (a) symmetrical case (b) exact Bragg case {compare to Fig. 14(a,b)} (Ref. 23 courtesy N. Holland Publishers).

Fig. 25. Kikuchi map for hcp crystals. The map is indexed in the Miller Bravais notation for directions and can be used to index any hcp crystal. This map exactly matches Ti and Ag_2Al. (Ref. 12 courtesy Phys. Stat. Sol.).

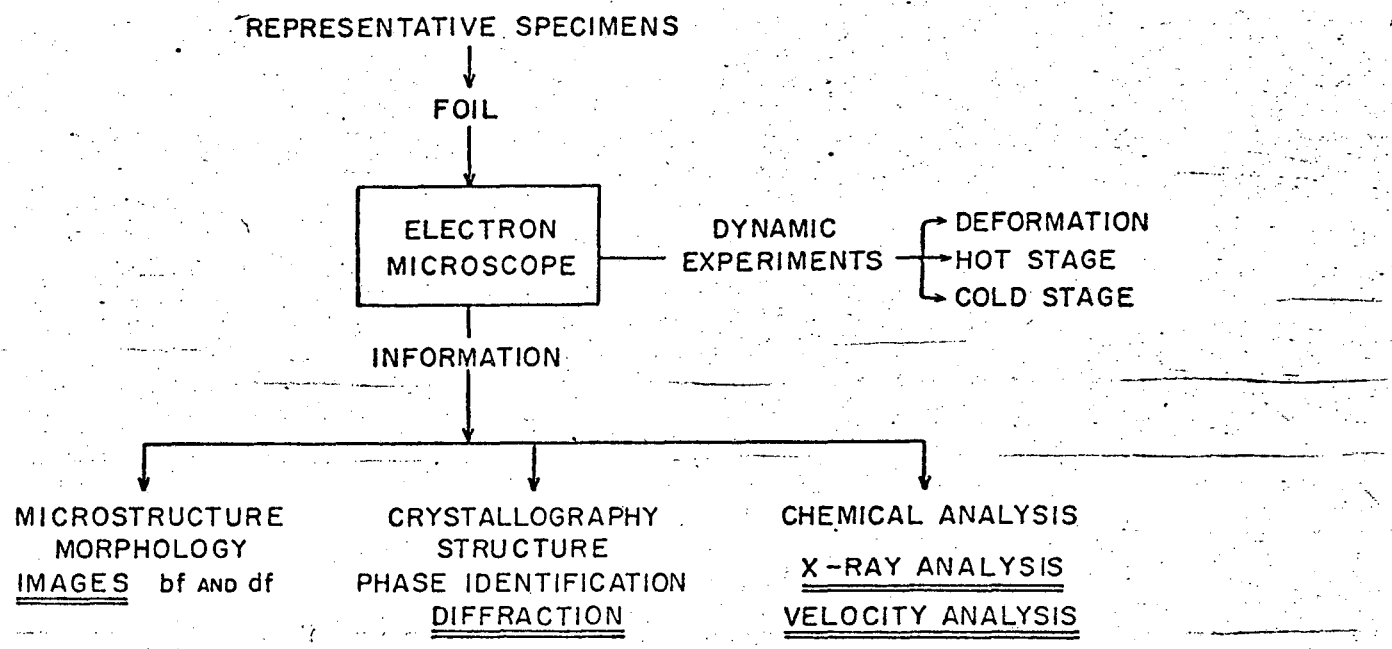

XBL 695-581

Fig. 1

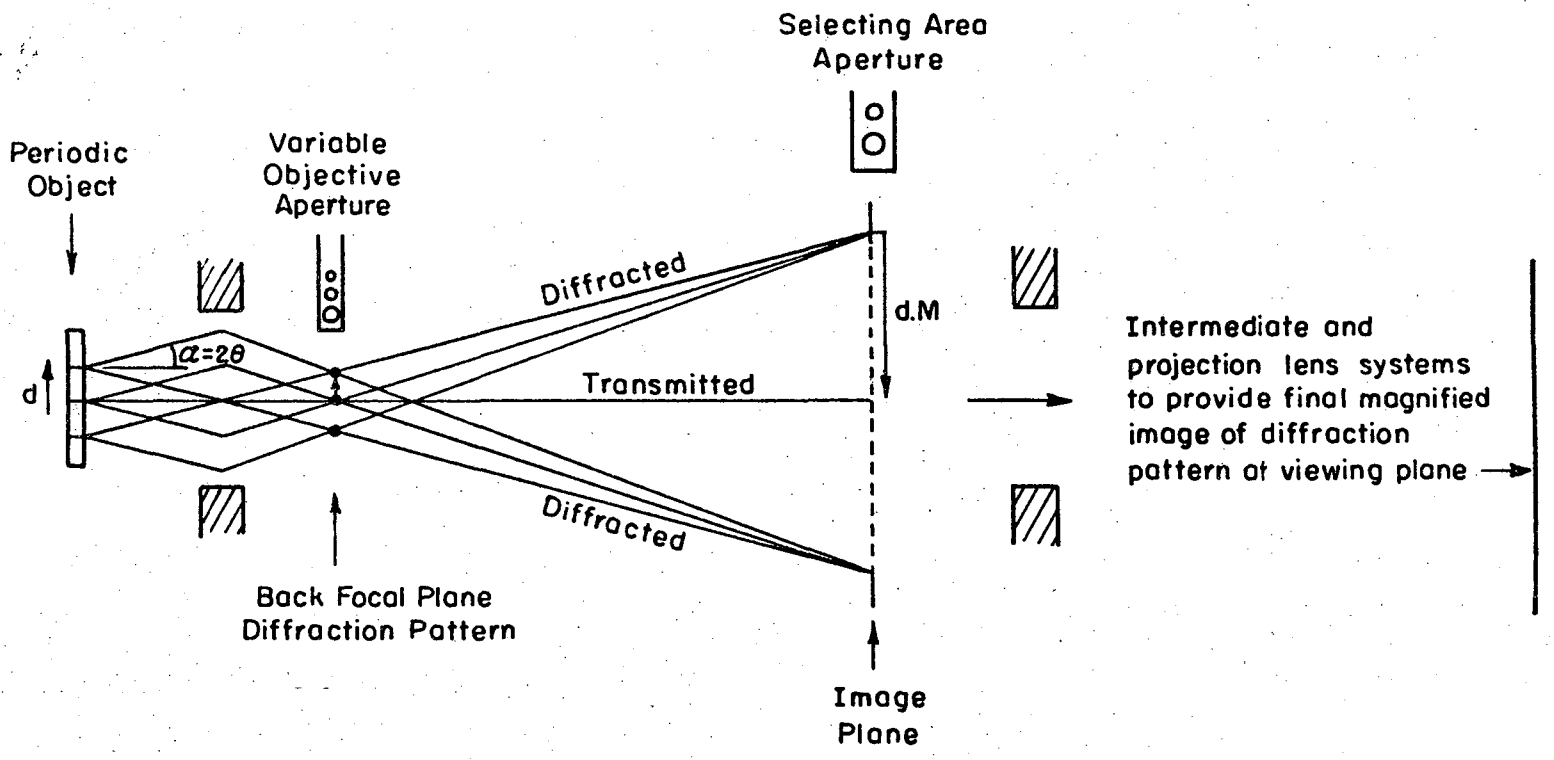
Selecting Area Aperture
Periodic Object
Variable Objective Aperture
Diffracted
d.M
α=2θ
d
Transmitted
Diffracted
Intermediate and projection lens systems to provide final magnified image of diffraction pattern at viewing plane
Back Focal Plane Diffraction Pattern
Image Plane
XBL 731-5662

Fig. 2a

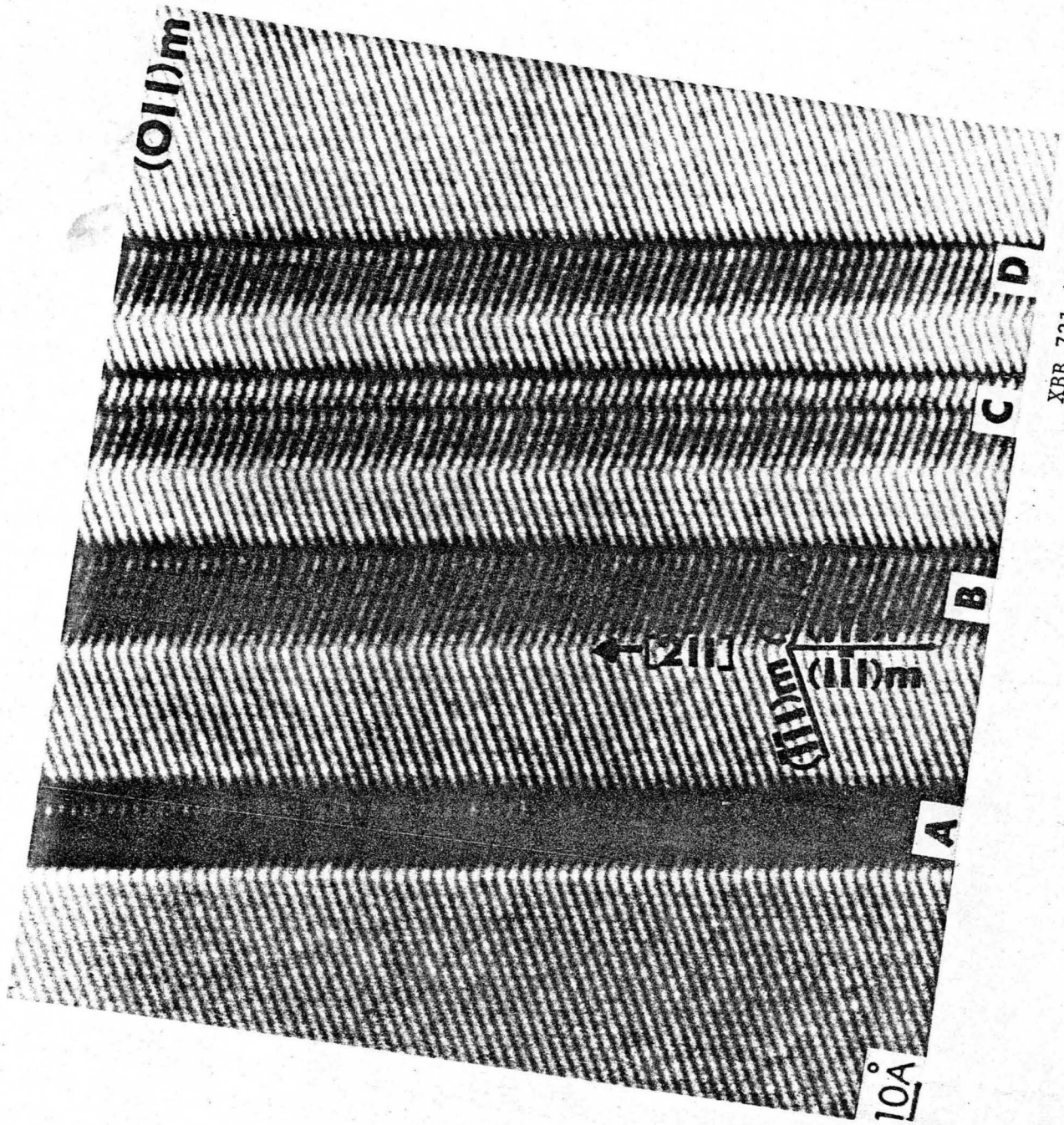

XBB 731-489

Fig. 2b

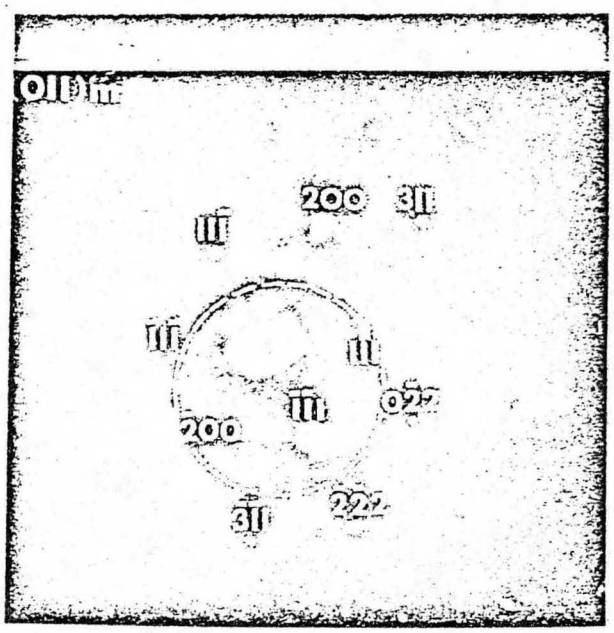

XBB 736-4061

Fig. 2c

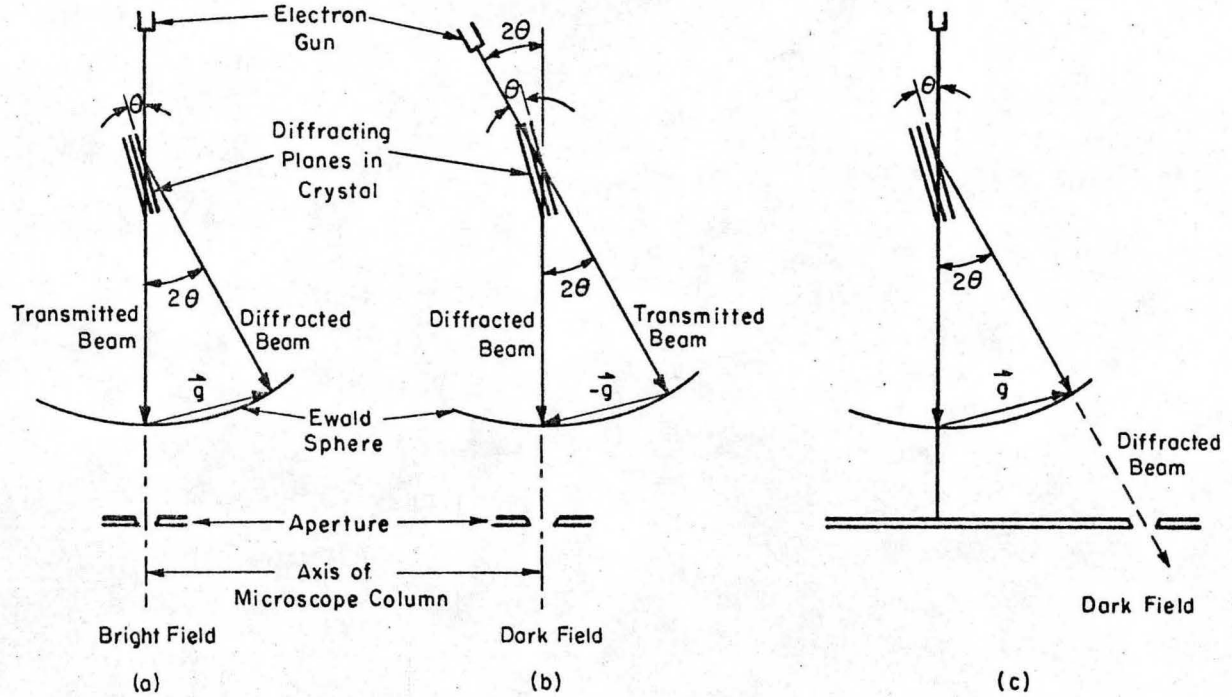
Electron Gun
2θ
θ
θ
Diffracting Planes in Crystal
Transmitted Beam
2θ
Diffracted Beam
Diffracted Beam
2θ
Transmitted Beam
g
-g
Ewald Sphere
Aperture
Axis of Microscope Column
Bright Field
Dark Field
(a)
(b)
θ
2θ
g
Diffracted Beam
Dark Field
(c)
XBL731-5661

Fig. 3

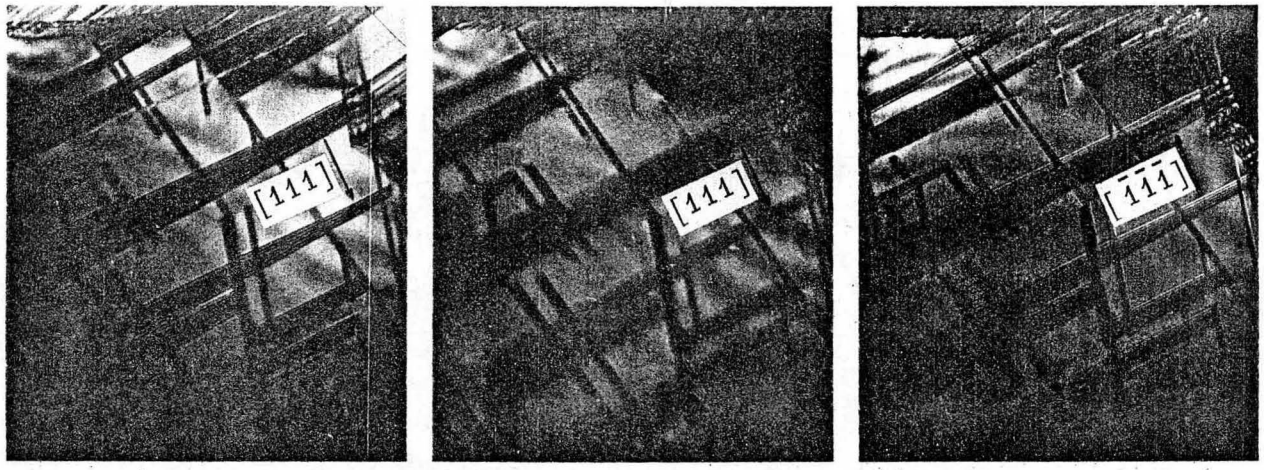

(a) (b) (c)

IM-1274

Fig. 4

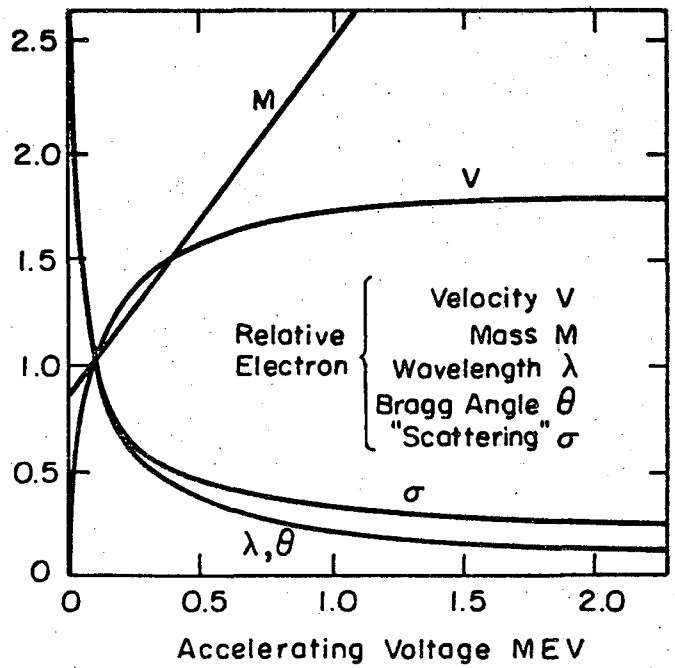
2.5
2.0
1.5
1.0
0.5
0
M
V
σ
λ,θ
Relative Electron
Velocity V
Mass M
Wavelength λ
Bragg Angle θ
"Scattering" σ
0
0.5
1.0
1.5
2.0
Accelerating Voltage MEV
XBL731-5666

Fig. 5

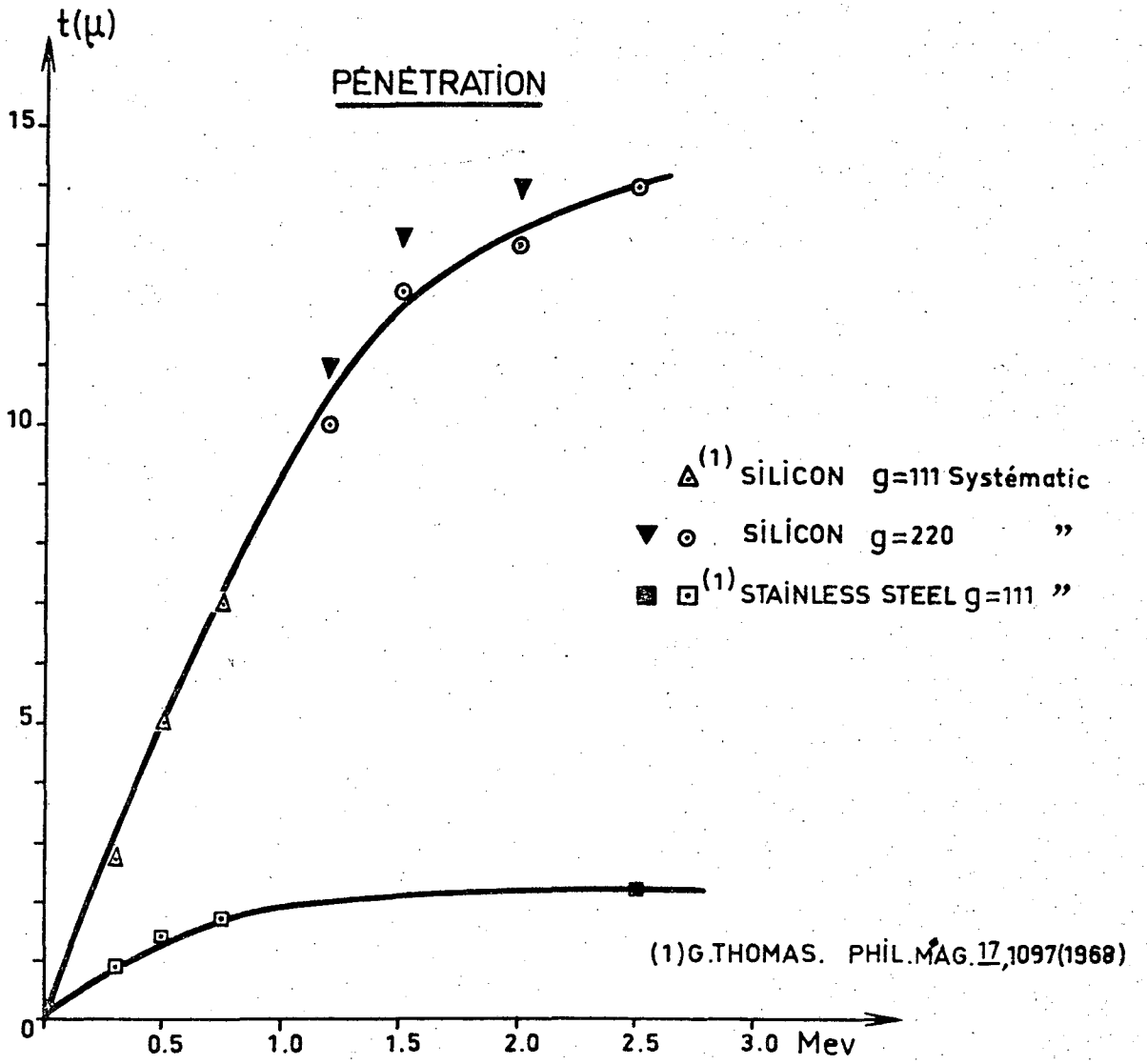

XBL 728-6771

Fig. 6

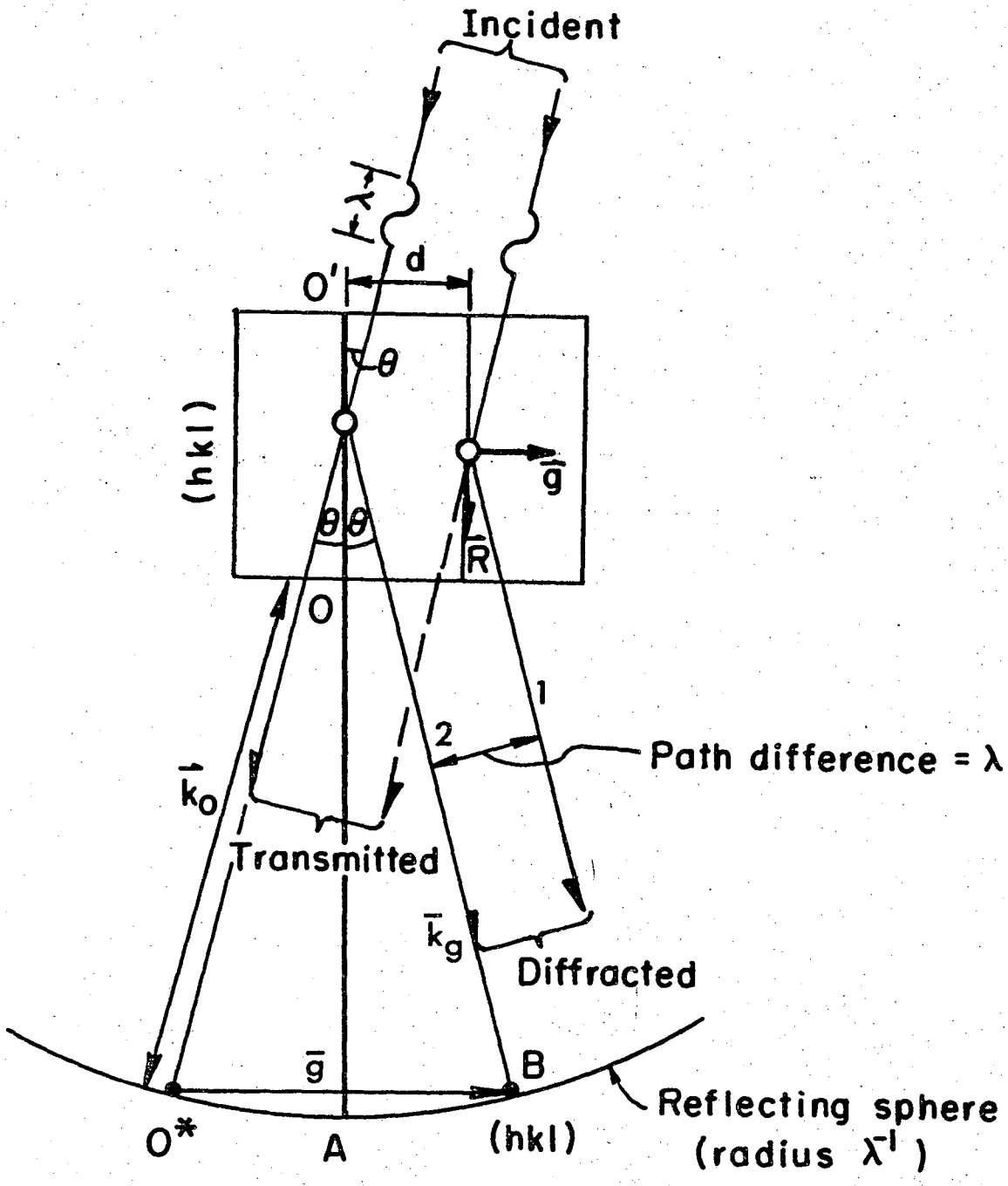

XBL 733-5832

Fig. 7

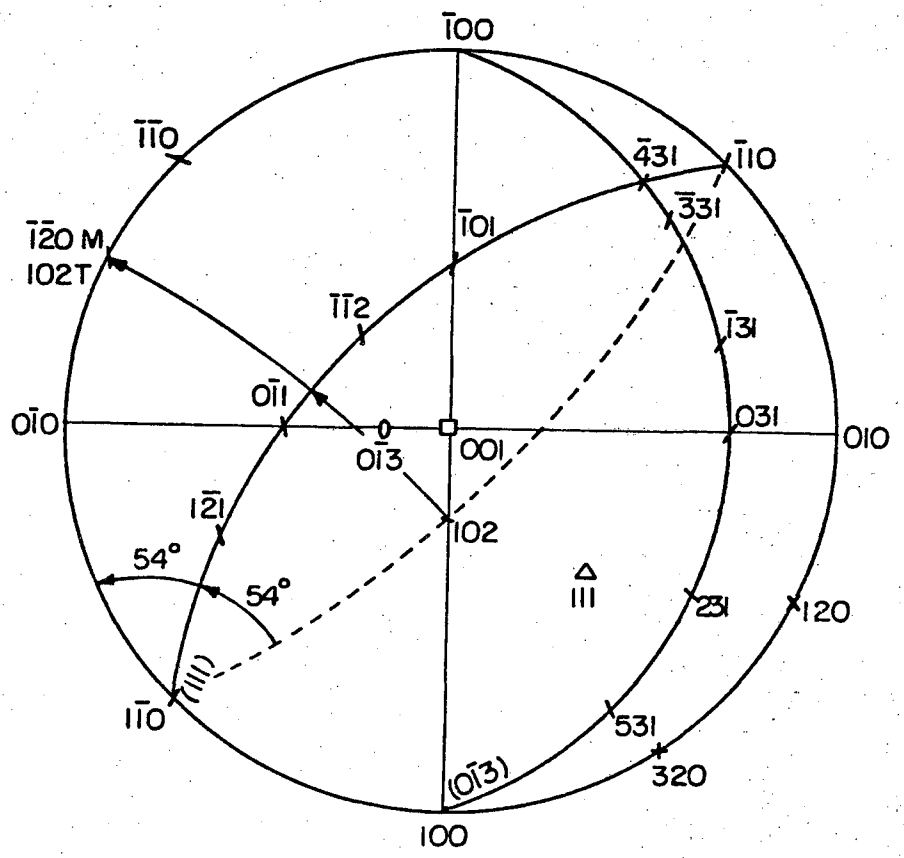

XBL 731-5663

Fig. 8

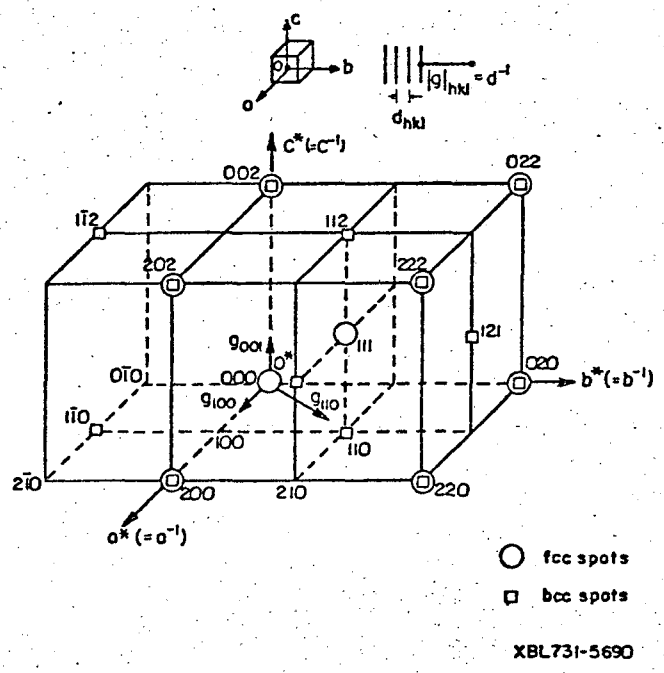
c
b
a
$|g|_{hkl} = d^{-1}$
d_{hkl}
$c^*(=c^{-1})$
002
022
$11\bar{2}$
112
202
222
121
g_{001}
000
0^*
111
020
$b^*(=b^{-1})$
$0\bar{1}0$
g_{100}
g_{110}
$1\bar{1}0$
100
110
$2\bar{1}0$
200
210
220
$a^*(=a^{-1})$
fcc spots
bcc spots
XBL731-5690

Fig. 9

Fig 9

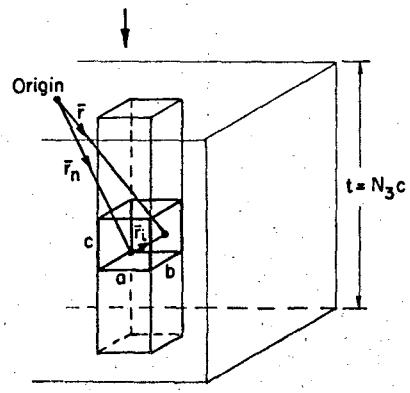

i

Fig. 10(b)

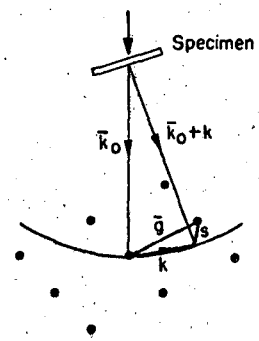

ii

Fig. 10(a)

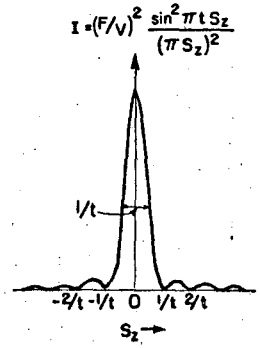

iii

Fig. 11

XBL731-5692

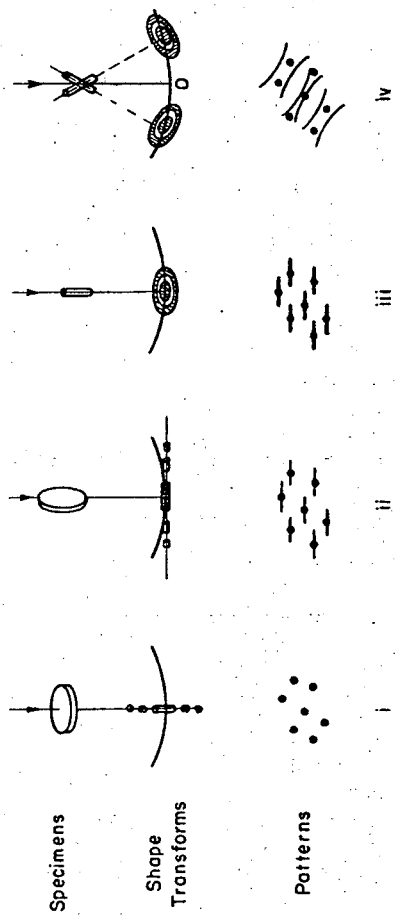
Specimens
Shape Transforms
Patterns
i
ii
iii
iv
XBL 731-5691

Fig. 12

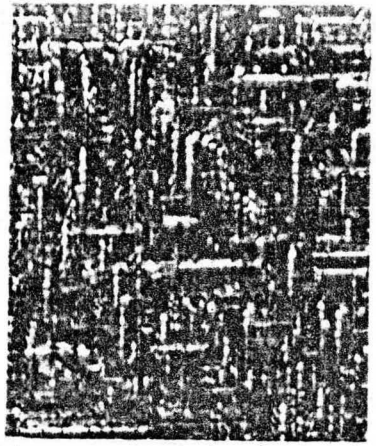

a

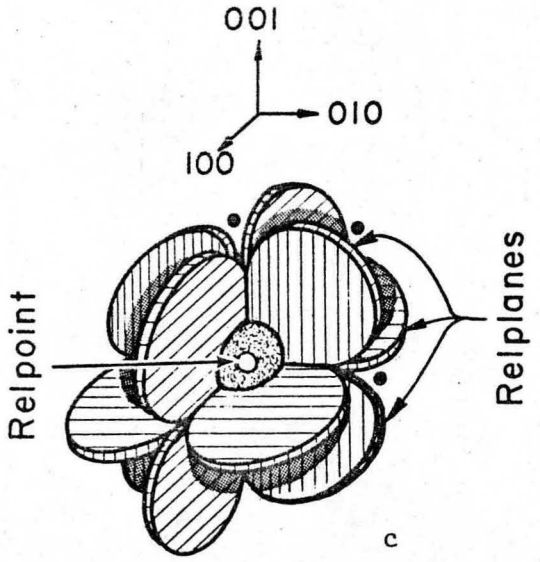

c

• Forbidden reflecting positions

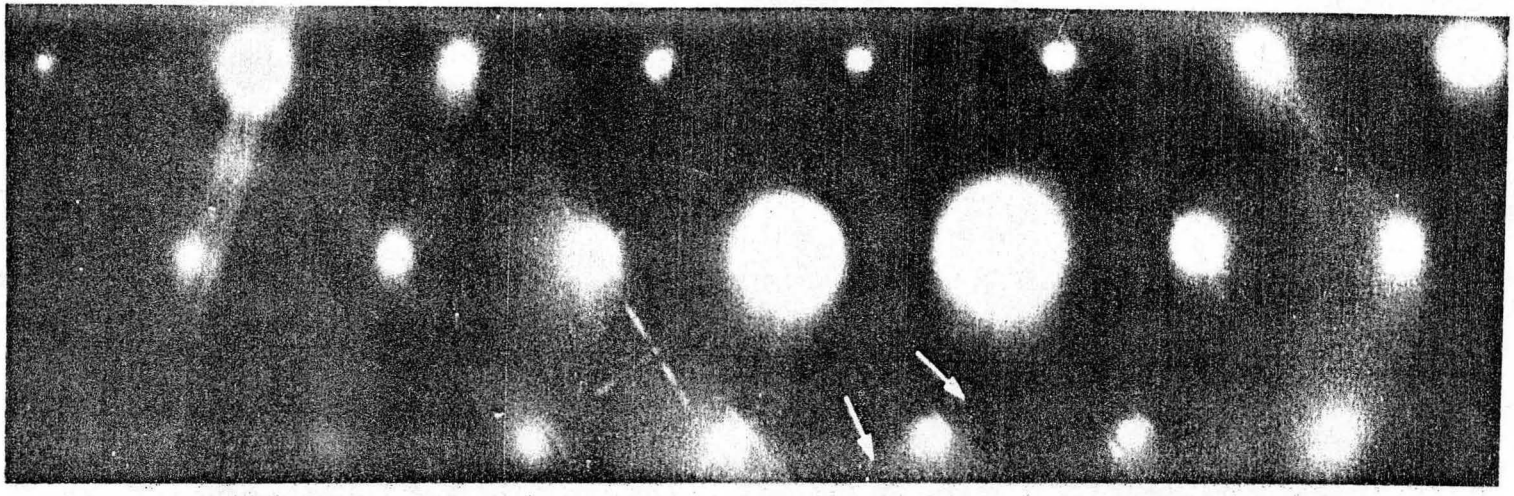

XBB 695-3419

b

Fig. 13

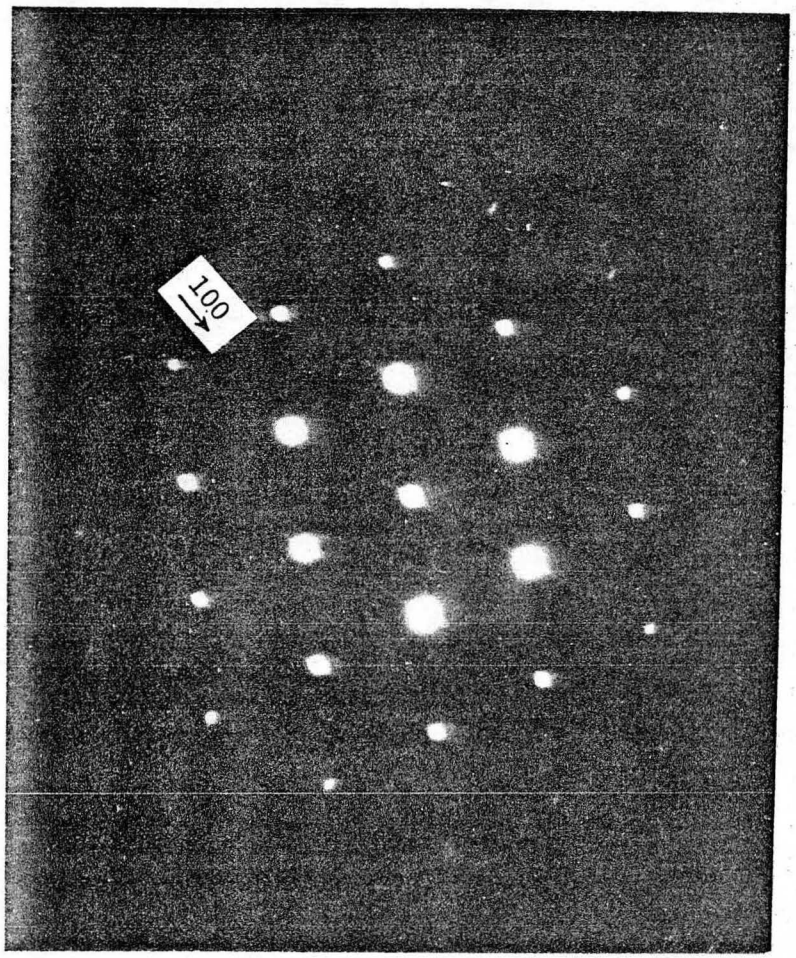

IM-1275

d

Fig. 13 cont.

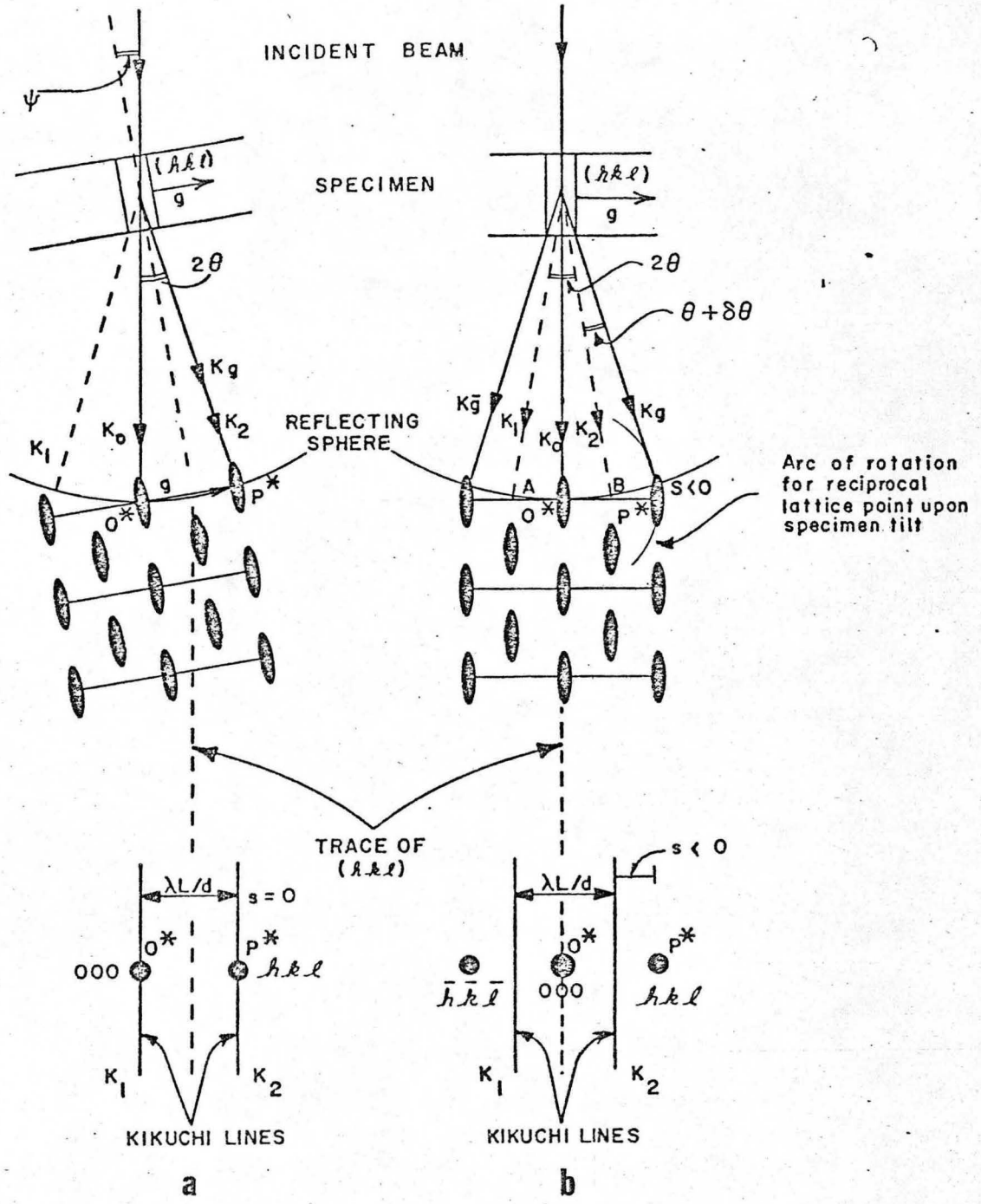

14

a, b

Fig. 14

MUB-8567

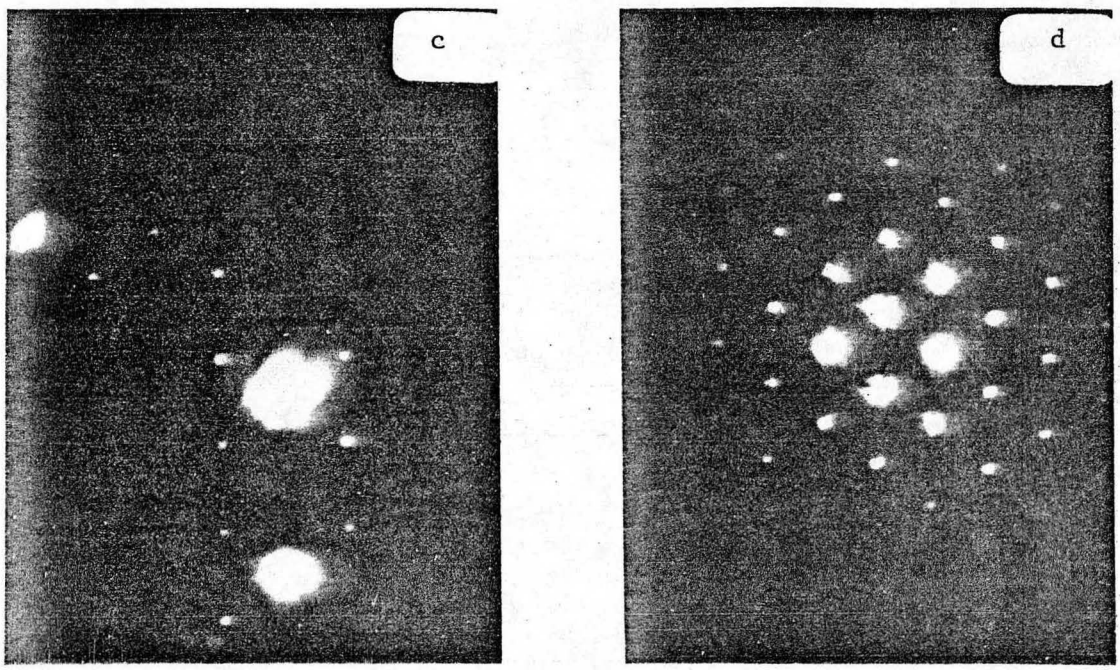

IM-1603
Top

Fig. 14 cont.

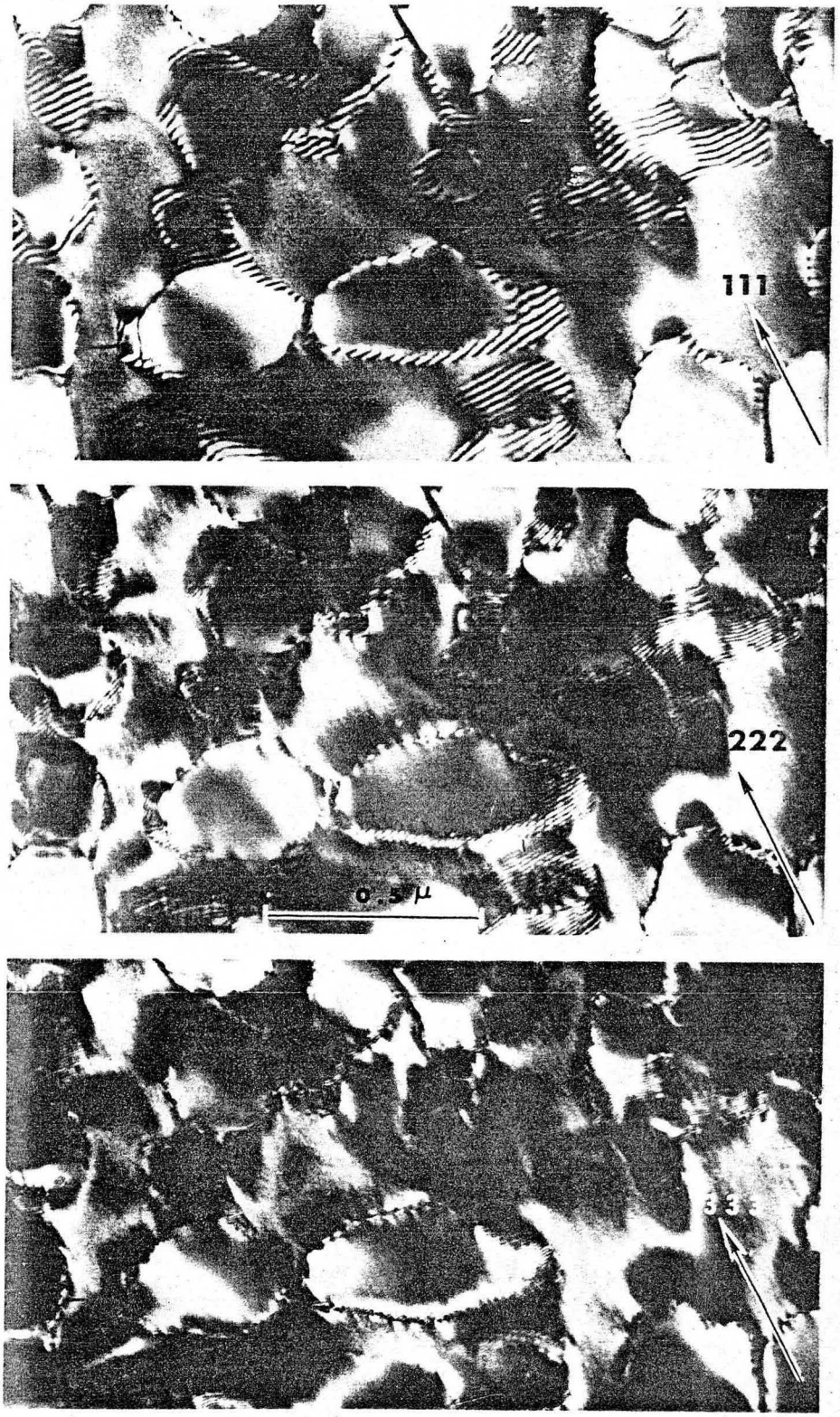

XBB 718-3549

Fig. 15

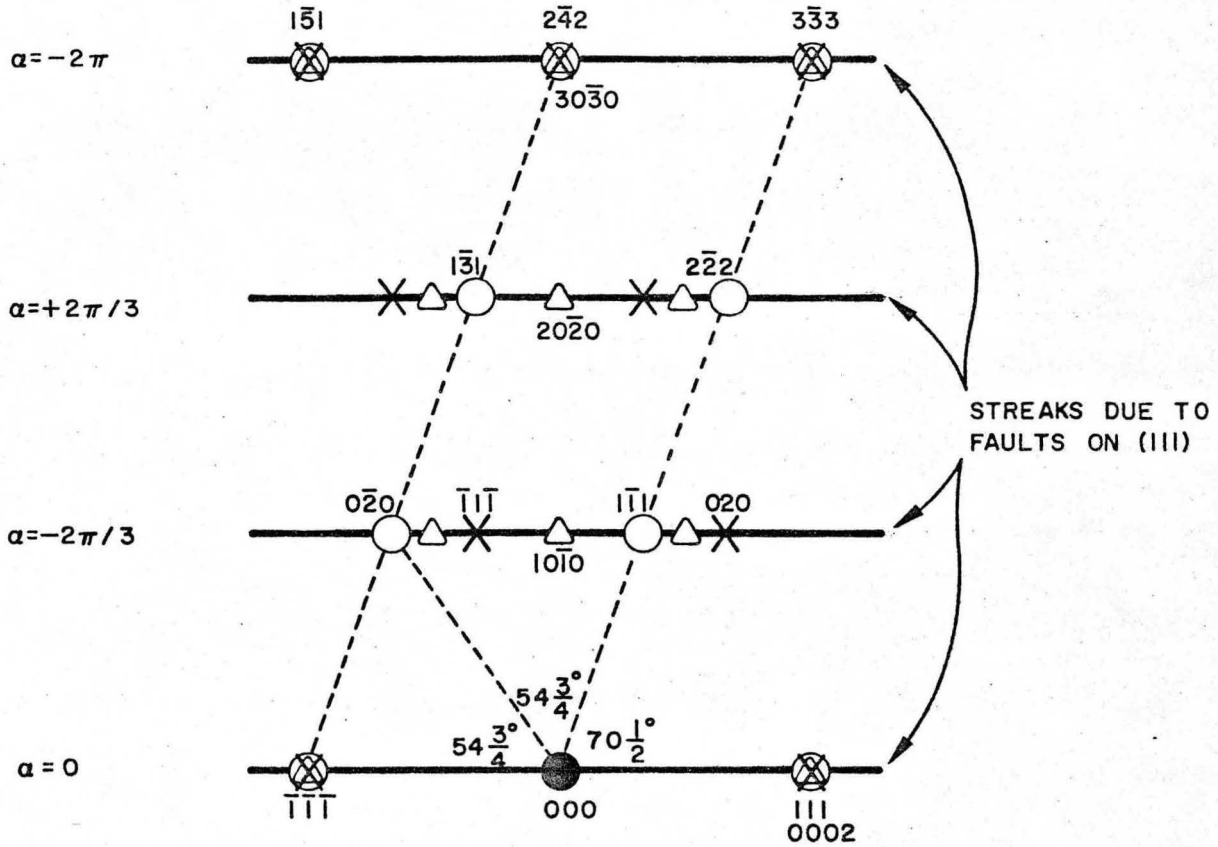

MUB-8568

Fig. 16a

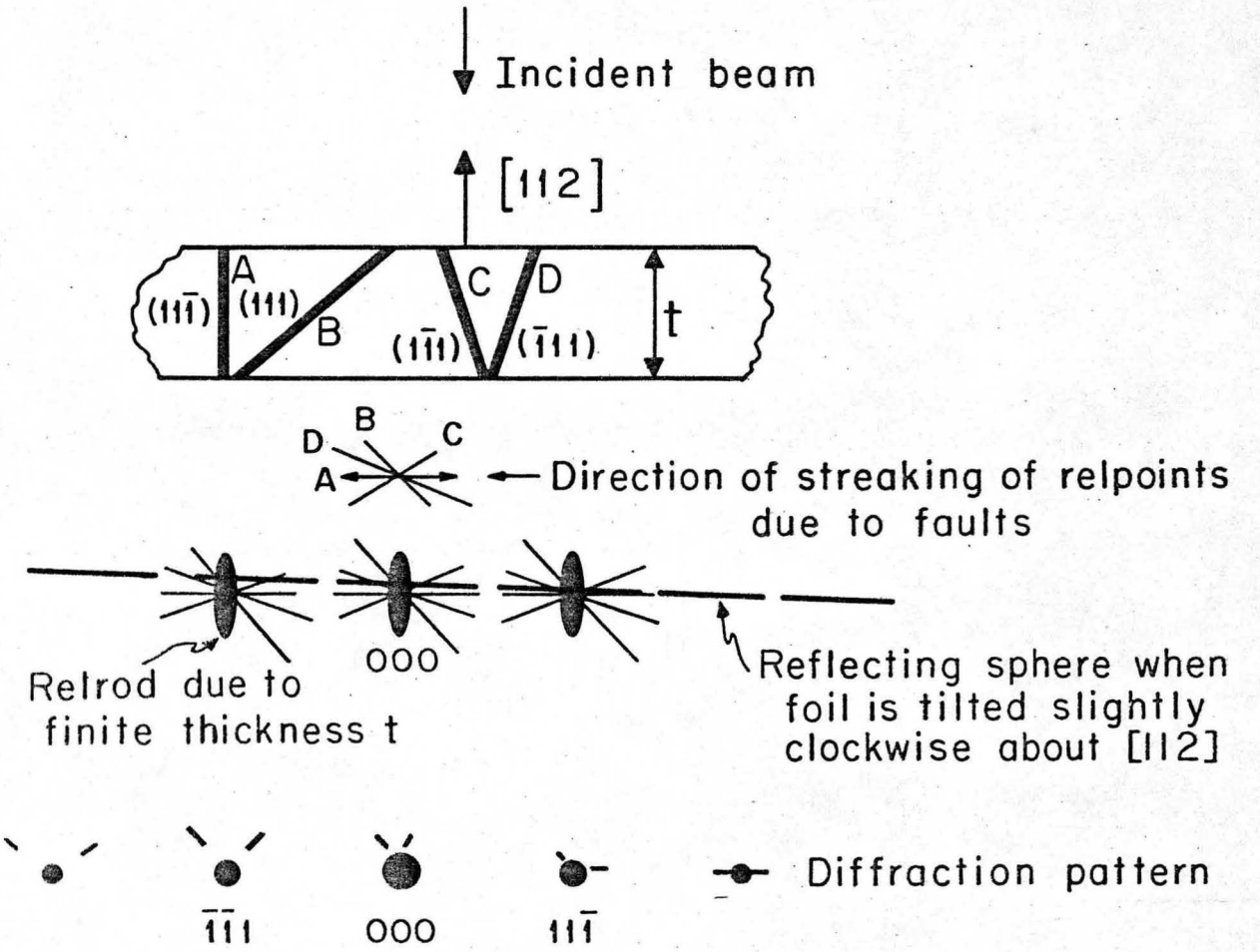

MUB-4504

Fig. 16b

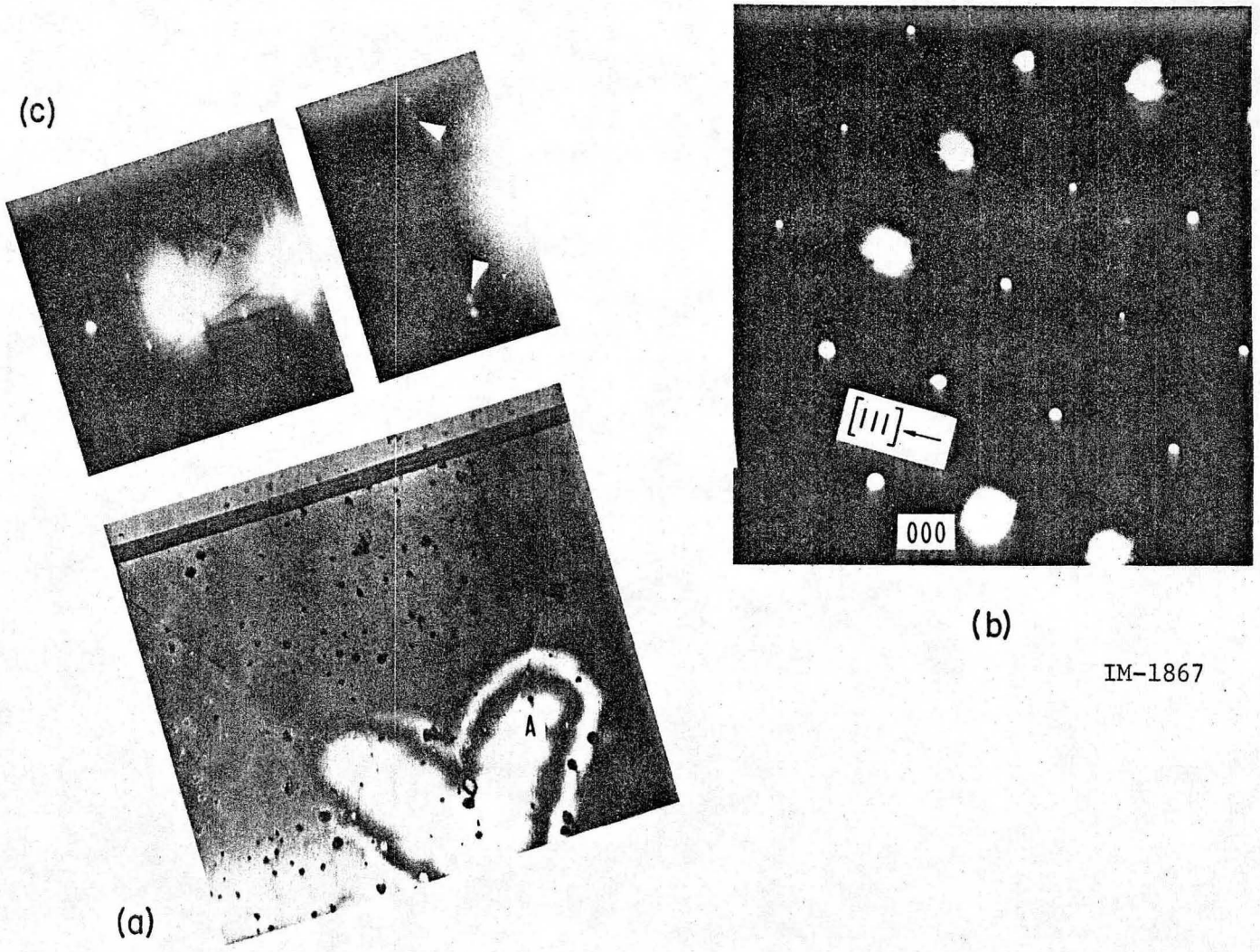

IM-1867

Fig. 17

(a)

(b)

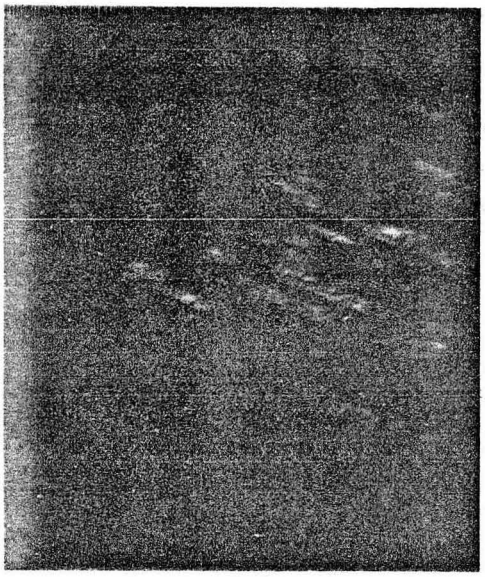

(c)

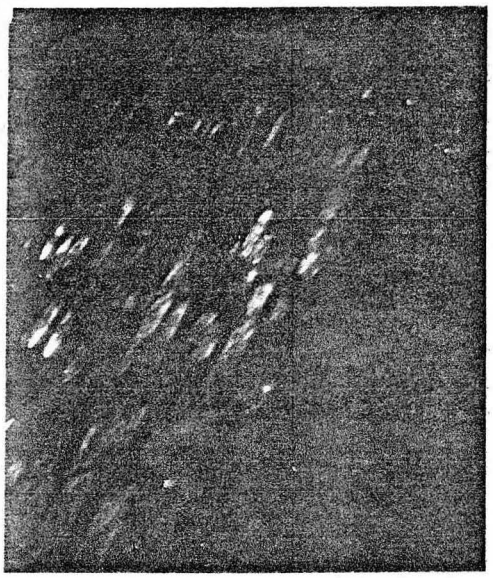

(d)

IM-829A

Fig. 18

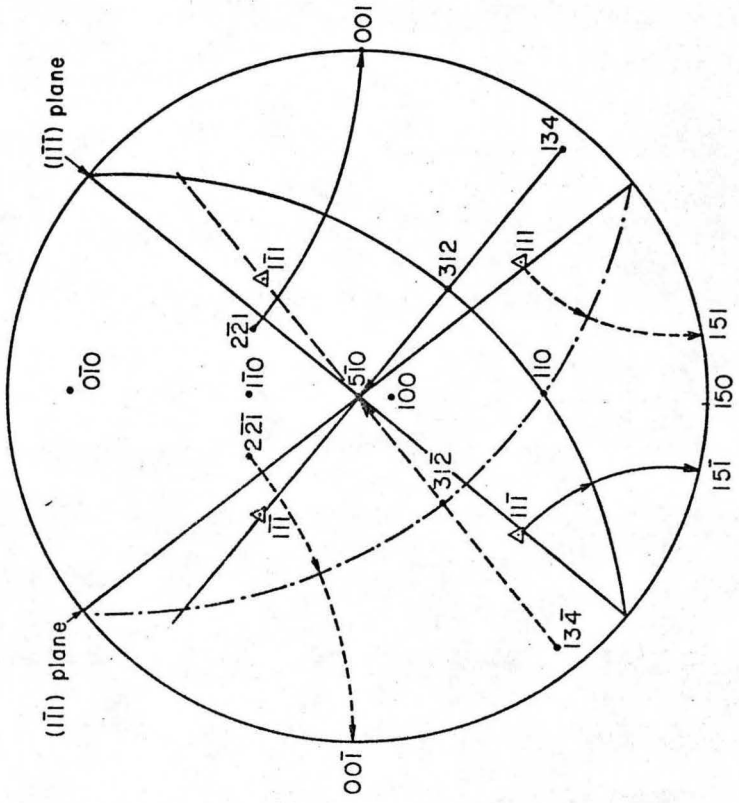
(1$\bar{1}\bar{1}$) plane
(1$\bar{1}$1) plane
001
00$\bar{1}$
0$\bar{1}$0
1$\bar{1}$1
2$\bar{2}$1
1$\bar{1}$0
2$\bar{2}$1
5$\bar{1}$0
100
3$\bar{1}$2
1$\bar{1}$1
134
3$\bar{1}$2
1$\bar{1}$1
110
151
150
15$\bar{1}$
13$\bar{4}$
MU-31436

Fig. 19

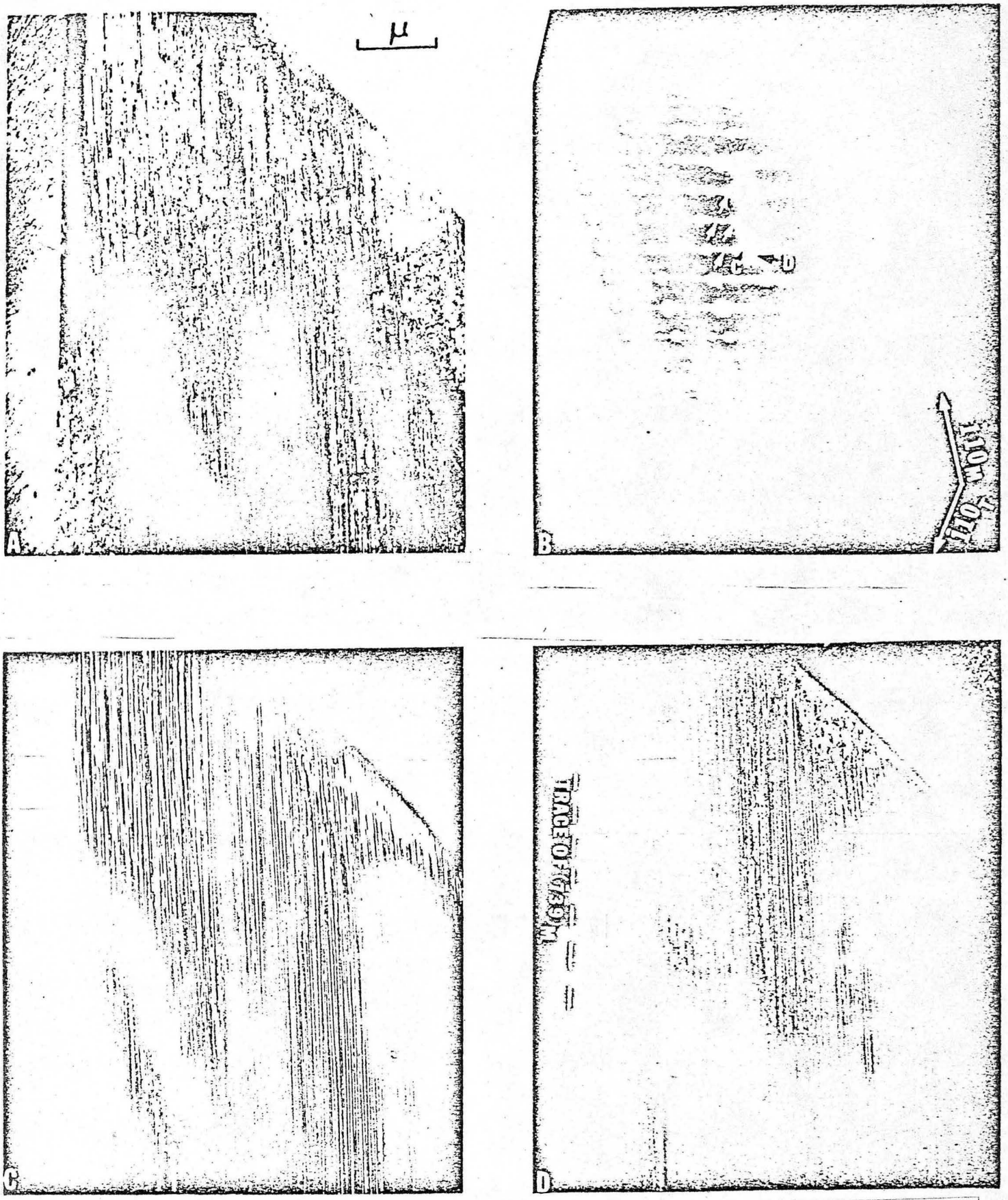

Fig. 20

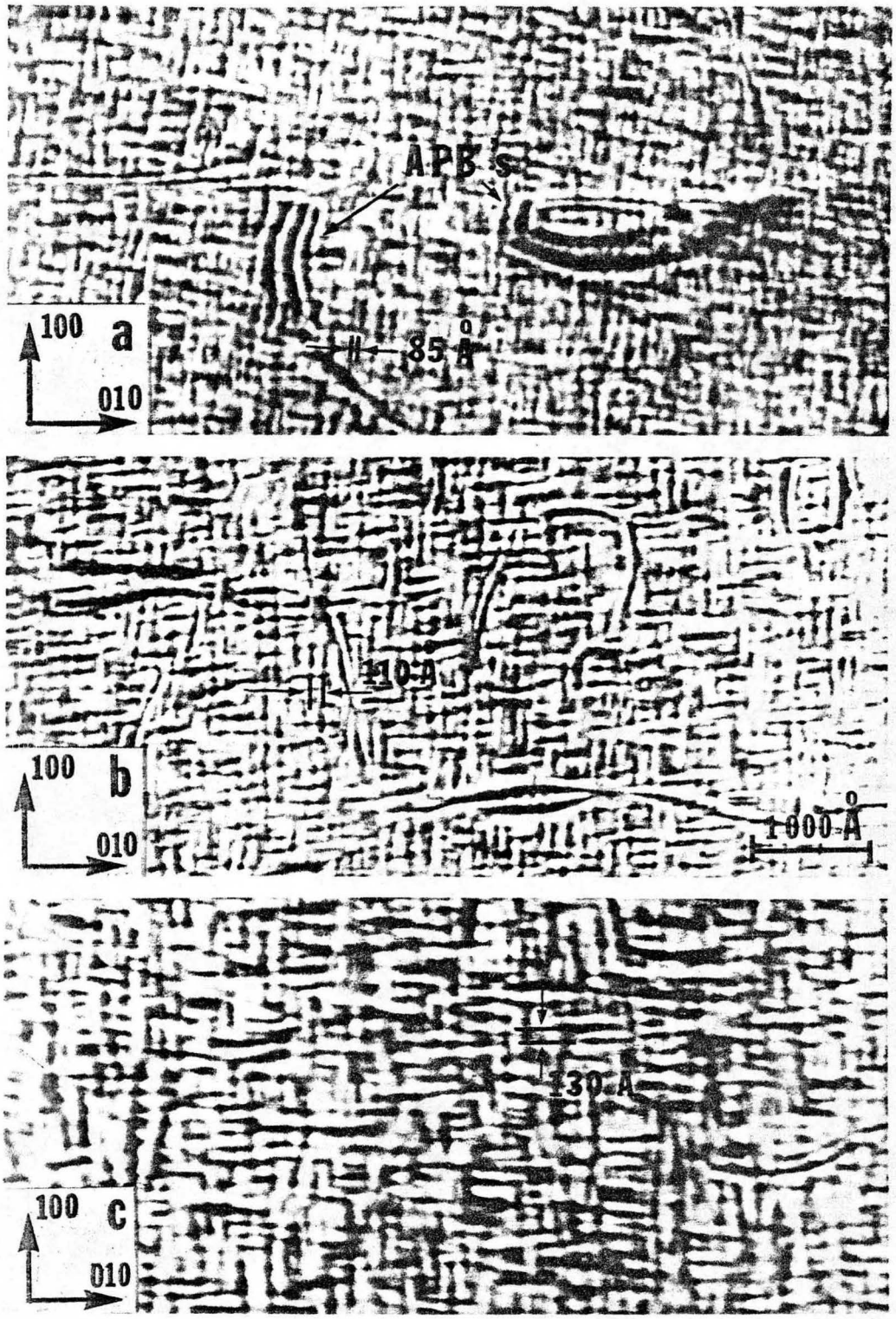

XBB 7210-5386

Fig. 21

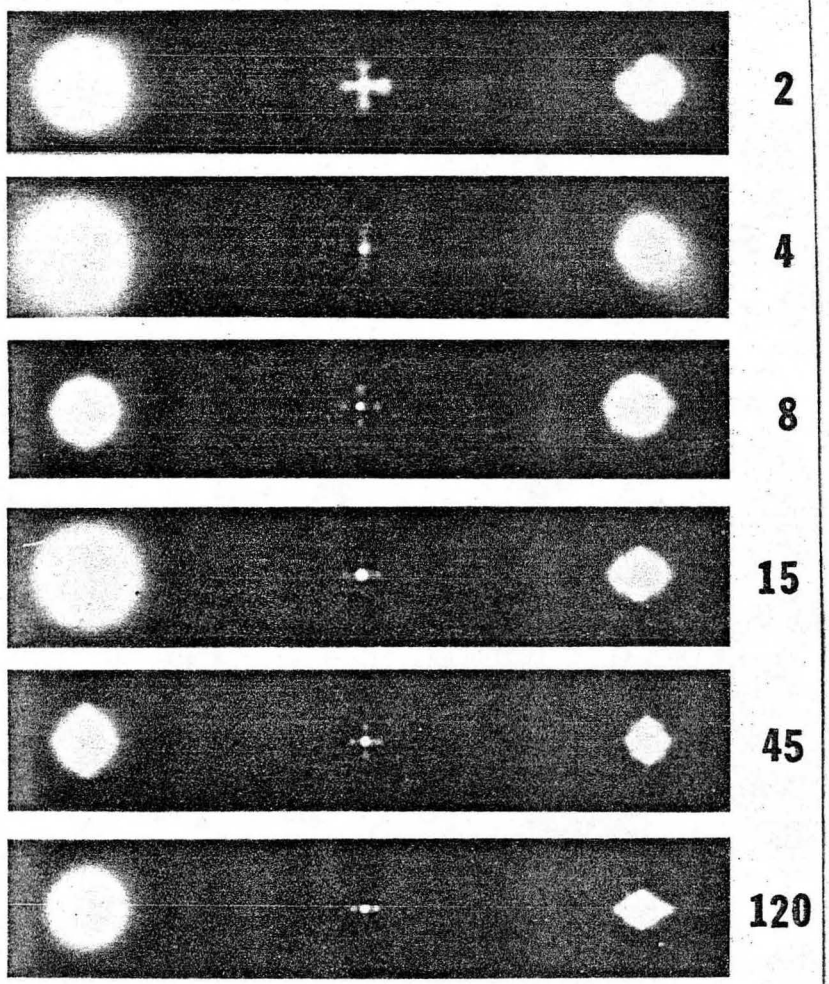

d XBB7210-5391

Fig. 21 cont.

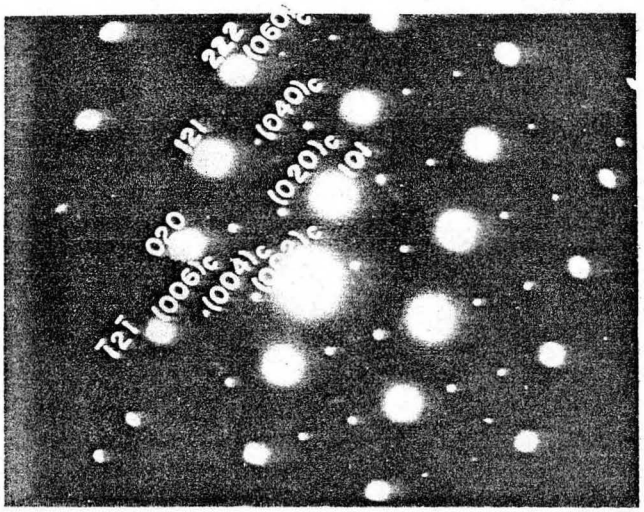

IM-1324

Fig. 22

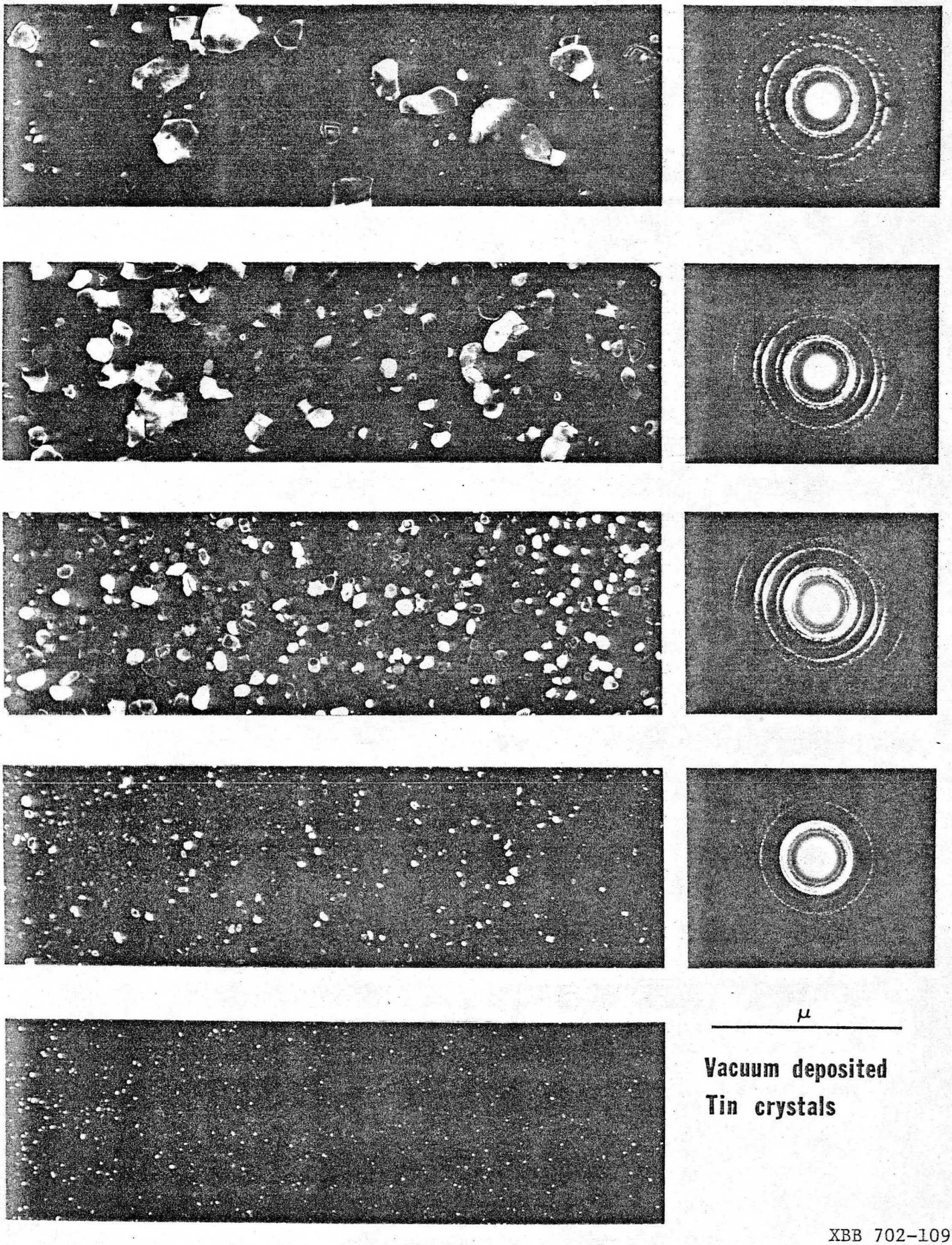

μ

Vacuum deposited
Tin crystals

XBB 702-1092

Fig. 23

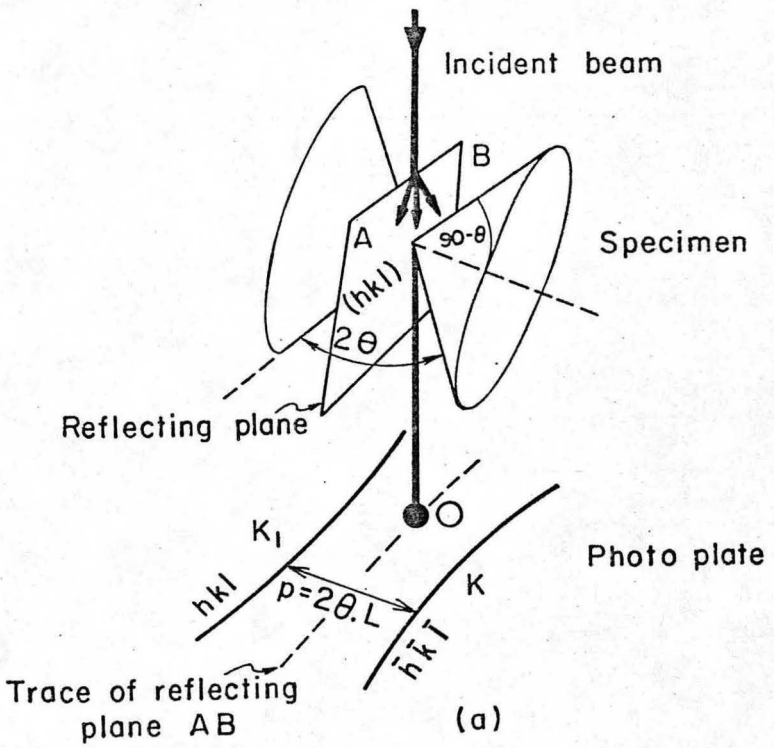

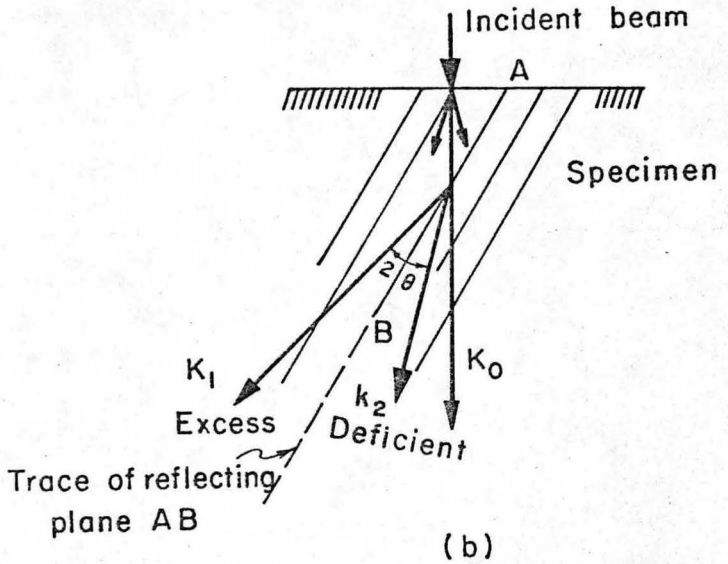

XBL695-2800

Fig. 24

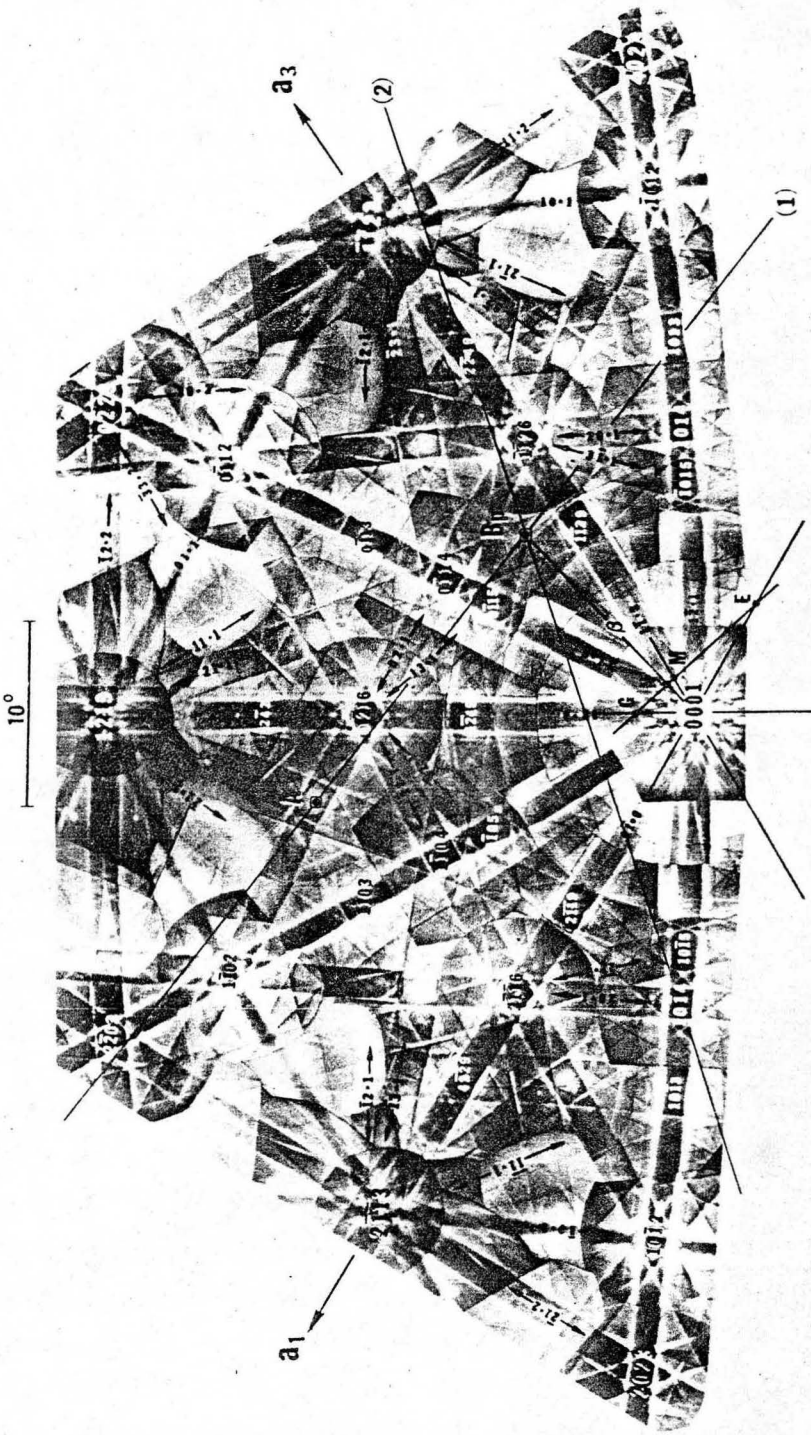

Fig. 25

TECHNICAL INFORMATION DIVISION
LAWRENCE BERKELEY LABORATORY
UNIVERSITY OF CALIFORNIA
BERKELEY, CALIFORNIA 94720